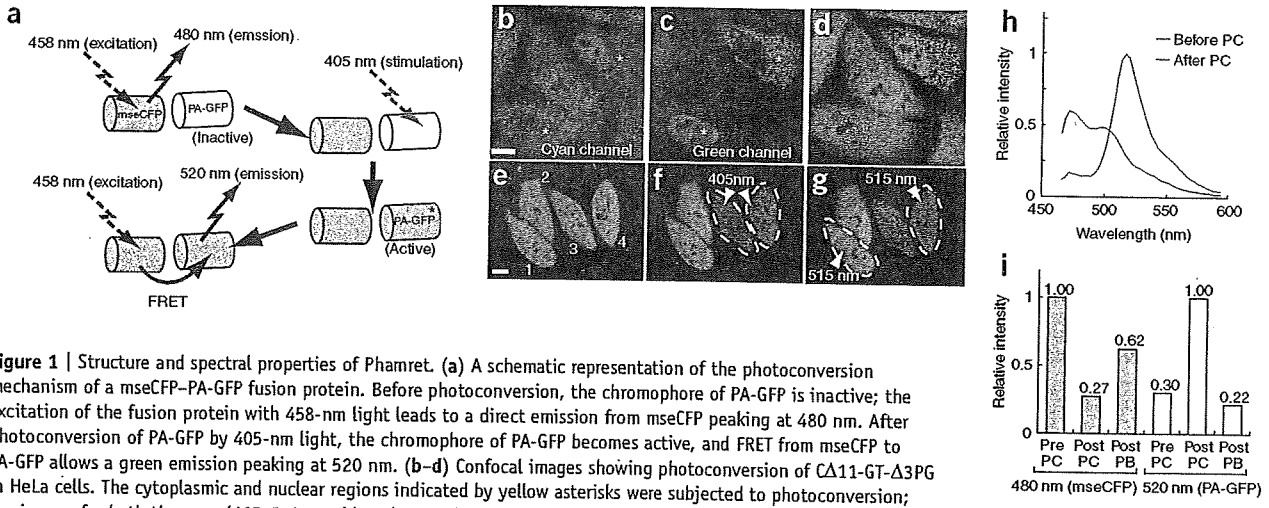


**Figure 1** | Structure and spectral properties of Phamret. (**a**) A schematic representation of the photoconversion mechanism of a mseCFP–PA-GFP fusion protein. Before photoconversion, the chromophore of PA-GFP is inactive; the excitation of the fusion protein with 458-nm light leads to a direct emission from mseCFP peaking at 480 nm. After photoconversion of PA-GFP by 405-nm light, the chromophore of PA-GFP becomes active, and FRET from mseCFP to PA-GFP allows a green emission peaking at 520 nm. (**b–d**) Confocal images showing photoconversion of CΔ11-GT-Δ3PG in HeLa cells. The cytoplasmic and nuclear regions indicated by yellow asterisks were subjected to photoconversion; the images for both the cyan (465–510 nm; **b**) and green (510–600 nm; **c**) fluorescence were taken. The images of mseCFP and PA-GFP were pseudocolored (cyan and red, respectively) and superimposed (**d**). (**e–g**) Pseudocolored images of CΔ11-GT-Δ3PG–expressing HeLa cells before photoconversion (**e**), after photoconversion (**f**) and after photobleaching (**g**). The regions surrounded by dashed yellow circles in **f** and **g** were photoconverted by 405-nm light stimulation and photobleached by 515-nm intense laser irradiation, respectively. Scale bars, 10 μm. (**h**) Emission spectra of Phamret in HeLa cells before and after photoconversion (PC). (**i**) Relative fluorescence intensity of mseCFP and PA-GFP before photoconversion (Pre PC), after photoconversion (Post PC) and after photobleaching (Post PB).



fluorescent proteins. The characteristic features of this method are (i) quick photostimulation time (0.25 ms); (ii) small light energy necessary for photostimulation (<1 W/cm$^2$ in case of Phamret); (iii) fast acquisition of fluorescence decay (4,100 Hz) by reciprocal line scanning; and (iv) consideration of photobleaching during fluorescence decay measurement.

## RESULTS

### Design and evaluation of Phamret

To develop a photoconvertible fluorescent protein that can be excited by the same wavelength in both pre- and post-photoconversion states, we designed a fusion protein composed of a CFP variant (mseCFP) fused to a PA-GFP[8] (**Fig. 1a**). We designed this fusion protein to emit cyan fluorescence (480 nm) in the pre-photoconverted state, which can be shifted to green fluorescence (520 nm) by UV light stimulation of PA-GFP into a FRET acceptor for the mseCFP donor (**Fig. 1a**). This approach requires a high FRET efficiency between mseCFP and activated PA-GFP; otherwise no or small changes in fluorescence emission can be observed after UV stimulation. To achieve a high FRET efficiency, we concatenated mseCFP containing a C-terminal 11-amino-acid truncation to PA-GFP with a 3-amino-acid truncation from the N terminus via a dipeptide (Gly-Thr) linker. The bacterially expressed chimeric protein (CΔ11-GT-Δ3PG) exhibited a fivefold increase in the emission ratio (520 nm/480 nm) upon brief photoactivation by 420-nm pulsed laser. When expressed in living mammalian cells, CΔ11-GT-Δ3PG was distributed uniformly in both the cytoplasm and the nuclei (**Fig. 1b–d**). Spectral imaging revealed that all fluorescent cells had an emission spectrum identical to that of mseCFP, whereas upon 405-nm laser stimulation, the fluorescence emission in the stimulated area quickly changed from cyan to green, indicative of complete maturation of both mseCFP and PA-GFP in CΔ11-GT-Δ3PG at 37 °C (**Fig. 1e–g** and **Supplementary Fig. 1a–f** online). Upon activation, green fluorescence increased 3.3-fold, and cyan fluorescence emission decreased 3.7-fold, resulting in an approximately 12.2-fold ratio change between the pre- and post-photoconverted states (**Fig. 1h,i**). To confirm that the photoconversion of CΔ11-GT-Δ3PG was indeed due to FRET from mseCFP to activated PA-GFP, we bleached the acceptor PA-GFP. The decrease in PA-GFP emission peak was accompanied by dequenching of the mseCFP signal (**Fig. 1g–i** and **Supplementary Fig. 1g–i**), demonstrating that the dominant mechanism of the fluorescence color change in CΔ11-GT-Δ3PG was caused by FRET between mseCFP and activated PA-GFP. Therefore, we named this fusion protein Phamret for photoactivation-mediated resonance energy transfer. The photoconversion of Phamret was achieved using a lower laser power density (<1 W/cm$^2$) than that for photobleaching. Accordingly, the quantum yield for photoconversion of Phamret was $2.7 \times 10^{-2}$, which was five times greater than that for the efficient highlighter, KikGR[15] ($4.7 \times 10^{-3}$). pH titration of Phamret revealed that a high dynamic range (>10-fold) was achieved in a neutral to alkaline environment (>pH 7), but it was strongly attenuated at acidic pH (**Supplementary Fig. 2a** online) and displayed a twofold dynamic range at pH 6.5. Phamret thus functions as a highlighter at physiological pH ranging from 6.5 to 8.0. Phamret was estimated to be a 53.4-kDa protein and is monomeric in living cells without displaying any unexpected binding to protein or proteolytic digestion (**Supplementary Fig. 2b–d**). Concordantly, Phamret in fusion with human β-actin and fibrillarin as well as targeting sequences for the Golgi bodies and the peroxisome showed an expected localization pattern (**Fig. 2a–d**) as reported previously[17–20]. In addition, the fusion proteins did not substantially perturb cellular functions such as cell division. Furthermore, all the fusion proteins tested underwent pronounced photoconversion by 405-nm laser illumination (**Fig. 2a–d**). Although we successfully labeled most of the proteins tested with Phamret, labeling of α-tubulin was unsuccessful (data not shown). Optimization of the amino-acid linker sequence and length between Phamret

and the protein of interest may resolve this problem. The properties of Phamret in comparison with other photoconvertible fluorescent proteins developed so far are shown in **Table 1**.

### Cellular application of Phamret

To demonstrate the applicability of Phamret to stably label the intracellular structures, we expressed Phamret in mitochondria and took time-lapse images after Phamret photoconversion in one region. During a 15-min recording, a long thread-like mitochondrion fused and divided frequently, dramatically changing the pattern of the mitochondria network (**Fig. 2e–h** and **Supplementary Video 1** online). In parallel with the changes in the mitochondria structure, the shifted fluorescence color in the photoconverted region spread out and entered a surrounding mitochondrion. In addition, the labeled region in the fused mitochondrion was exchanged until it came to equilibrium at the intermediate color, indicating conjugation of the mitochondrial matrix and diffusion of the material in the fused mitochondrion.

We also observed positioning of chromosomes during mitosis in living mammalian cells. We labeled chromosomes in HeLa cells by expressing a histone 2B–Phamret fusion protein (H2B-Phamret). Owing to the very low dissociation rate of H2B from chromatin[21], the photoconverted marking remained detectable for many hours, allowing imaging of the dynamics of labeled chromosomes[22]. Just before mitosis, we photoconverted the nuclear halves and performed time-lapse imaging. In most cells (82%, $n = 14$), the global pattern of the mother cells was transmitted to the two daughter nuclei in G1 phase in a mirror-symmetric fashion (**Fig. 2i,j** and **Supplementary Video 2** online), indicating the heritability of chromosomal positions during cell division as previously shown by FRAP analysis using fluorescent protein tags in normal rat kidney cells[22].

### Visualization of rapid protein dynamics using Phamret

All photoconvertible fluorescent proteins described to date undergo a change in excitation wavelength in addition to the shift in

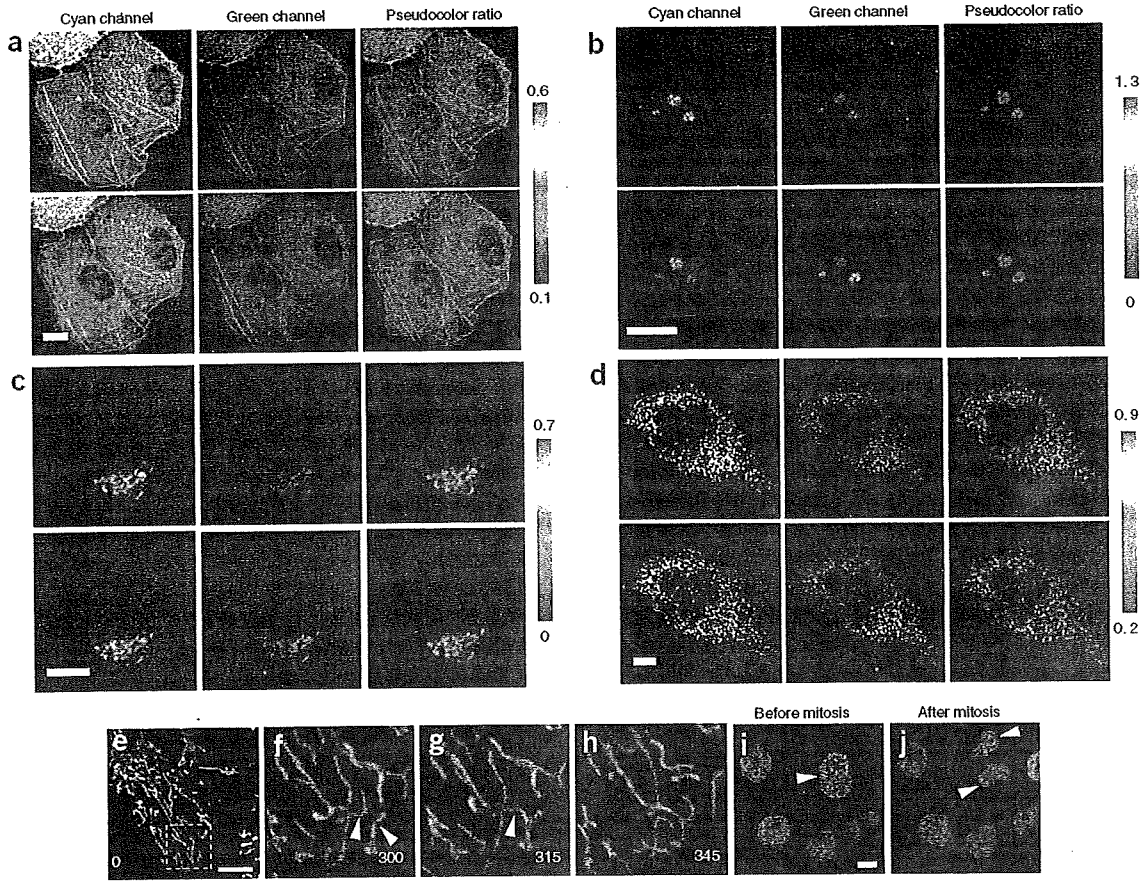


**Figure 2** | Photoconversion of Phamret fusion protein in living cells. (**a–d**) Confocal fluorescence images of HeLa cells expressing Phamret fused to actin (**a**), fibrillarin (**b**), Golgi body localizing signal (**c**) and SKL tripeptide for peroxisome localization (**d**) before photoconversion (top) and after photoconversion (bottom) in the selected area, as shown in red (bottom right). The cyan channel, green channel and pseudocolored emission ratio (green to cyan) images are shown. Color bars represent green-to-cyan intensity ratio. (**e–h**) To track mitochondria, Phamret-expressing mitochondria in the selected area (as shown in red in **e**) were subjected to photoconversion (**e**). A yellow dashed box in **e** shows the region used for time-lapse imaging. Representative images taken at 300 s (**f**), 315 s (**g**) and 345 s (**h**) after photoconversion are shown. The yellow and white arrowheads in **f** indicate two mitochondria that were about to fuse. Arrowhead in **g** indicates the point of mitochondrial fusion, which was followed by spreading of Phamret protein in the fused mitochondrion (**h**). (**i,j**) Tracking of H2B-Phamret during mitosis. Half of the nucleus (arrowhead) being photoconverted just before mitosis (red; **i**). The daughter nuclei (arrowheads) show the preserved color pattern (**j**). Scale bars, 10 μm.

**Table 1** | Properties of known photoconvertible proteins

| Protein | Fluorescence color: Before photoconversion | Fluorescence color: After photoconversion | Observed wavelength[a] (nm): Excitation | Observed wavelength[a] (nm): Emission | Stimulation: Wavelength (nm) | Stimulation: Power density (W/cm²) | Fluorescence increase in ratio | Oligomeric status | Ref. |
|---|---|---|---|---|---|---|---|---|---|
| Phamret | Cyan | Green | 458 | 475 | 405 | $<1^b$ ($\Phi_{PC} = 2.7 \times 10^{-2}$)[b] | ~15[b] | Monomer | |
| | | | 458 | 517 | | | | | |
| PS-CFP | Cyan | Green | 435 | 468 | 405 | 5–10 | ~1,500 | Monomer | 14 |
| | | | 490 | 511 | | | | | |
| Kaede | Green | Red | 488 | 518 | 405 | 1.3 | ~2,000 | Tetramer | 12 |
| | | | 543 | 580 | | | | | |
| KikGR | Green | Red | 488 | 517 | 405 | ~1 ($\Phi_{PC} = 4.7 \times 10^{-3}$) | NS | Tetramer | 15 |
| | | | 543 | 593 | | | | | |
| EosFP | Green | Red | 488 | 516 | 405 | NS | NS | Tetramer | 13 |
| | | | 543 | 581 | | | | | |
| d2EosFP | Green | Red | 488 | 516 | 405 | 500 | NS | Dimer | 13 |
| | | | 543 | 581 | | | | | |
| mEosFP | Green | Red | 488 | 516 | 405 | NS | NS | Monomer | 13 |
| | | | 543 | 581 | | | | | |
| Dendra | Green | Red | 488 | 505 | 488 | 1.5 | ~1,500–4,500 | Monomer | 16 |
| | | | 543 | 575 | 405 | 0.6 | | | |
| Cy11.5 | Yellow | Cyan | 440 | 527 | 515 (bleaching) | $>10^b$ | NS | Monomer | 28 |
| | | | 440 | 476 | | | | | |

$\Phi_{PC}$, quantum yield for photoconversion. NS, not stated.
[a]Wavelength of excitation light for live imaging by microscopy and peak of emission spectrum. [b]Measured in our laboratory. A laser power meter was used to measure total power of the light after the objective lens. Light power density was estimated by dividing the total power by the area of the illuminated region.



emission wavelength upon photoconversion, and thus require measurement in dual excitation–dual emission mode. Generally, two different excitation wavelengths are alternated to obtain images both before and after photoconversion. This is unfavorable for observing rapidly diffusing molecules because of the acquisition time lag between two images. Even if we excite simultaneously the two states of photoconvertible fluorescent proteins, it is impractical because two lasers must be aligned to the same confocal spot by bringing two laser beams to a perfect and stable overlap. The single excitation property of Phamret overcomes this problem, but it may be possible to measure the presently available dual-excitation photoconvertible fluorescent proteins in single-excitation mode also. To address this, we compared the photoconversion contrast of Phamret with the dual-excitation photoconvertible fluorescent proteins, tandem dimer Dendra (td-Dendra), which is comparable in size to Phamret[16]. We expressed both proteins in HeLa cells, photoconverted them by 405-nm laser irradiation and simultaneously measured the change in fluorescence intensity of both pre- and post-photoconversion states at the frame rate of 41 Hz using an appropriate excitation wavelength for each. At the first frame image after photoconversion, Phamret showed a 1.3-fold decrease and 2.4-fold increase in cyan and green fluorescence, respectively, yielding a 3.1-fold change in the emission ratio (**Supplementary Fig. 3a** online). The slower decrease in green fluorescence may be due to the photobleaching of PA-GFP moiety in Phamret. In contrast, td-Dendra had a 1.4-fold decrease in green fluorescence and no change in red fluorescence just after photoconversion, resulting in smaller contrast than for Phamret (**Supplementary Fig. 3b**). These results indicate that when using the single excitation–dual emission mode for fast frame acquisition, Phamret promises a higher contrast than Dendra. To further evaluate this,

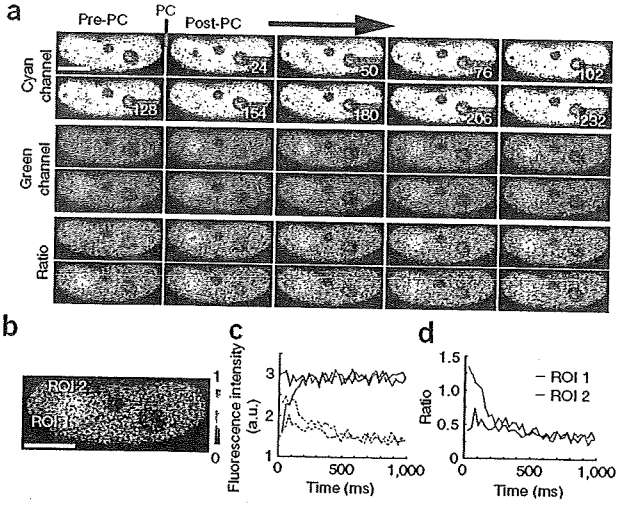


**Figure 3** | Visualization of rapid protein dynamics using Phamret. (**a**) Confocal images of donor CFP (top), acceptor PA-GFP (middle) and pseudocolored emission ratio (green/cyan; bottom) showing diffusion of photoconverted PP2Cγ-Phamret. Images were taken every 26 ms. (**b**) A magnified view of the first image just after photoconversion. The white circles (diameter 1.10 μm) represent ROIs used for intensity calculation. ROI 1 was set on the photoconverted circular region (diameter 1.38 μm). ROI 2 was placed outside of the photoconverted region. Distance between the centers of two ROIs is 2.1 μm. (**c**) Time course of cyan (solid line) and green (dashed line) fluorescence intensity of Phamret in ROI 1 (red) and ROI 2 (blue). (**d**) Time course of green to cyan emission ratio in ROI 1 and ROI 2. Scale bars, 10 μm.

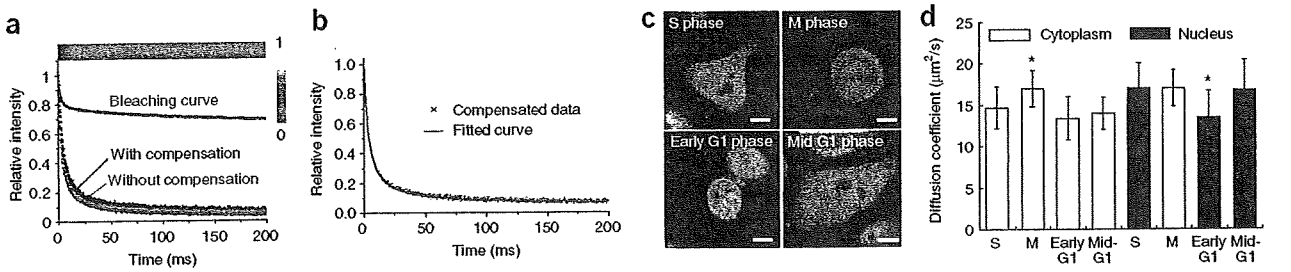


**Figure 4** | Determination of diffusion coefficient of Phamret by FDAP. (**a**) Line-scanned images of photoconverted Phamret in solution were taken, and the kymographs of the images are shown in pseudocolor (top). Color bar indicates normalized fluorescence intensity. Average fluorescence decay curves in the solution were calculated (bottom). The blue curve represents the bleaching of photoconverted Phamret during image acquisition. (**b**) The compensated fluorescence decay curve determined by equation (3). (**c**) Fluorescence images of a cell at the indicated cell-cycle stages used for FDAP measurements. Scale bar, 10 μm. (**d**) Diffusion coefficient of Phamret in the cytoplasm and the nucleus at the indicated cell-cycle stages. In the case of M phase, the same data are shown (light gray bars) because the cytoplasm and nucleus cannot be distinguished due to the disappearance of the nuclear membrane. Asterisks (*) indicate the cell phase where the diffusion coefficient is significantly different from other phases in either the cytoplasm or nucleus, respectively. Error bars are s.d. ($n > 10$). Validity of the differences was statistically confirmed by one-way analysis of variance (ANOVA) and defined as significant at $P = 4.0 \times 10^{-6}$ and $4.1 \times 10^{-4}$, respectively. Differences between cytoplasm and nucleus in S and G1 phase were also confirmed by using two-sided *t*-test ($P = 0.005$ and 0.008) with significance level $\alpha = 0.05$.



we examined a PP2Cγ-Phamret fusion protein in the nucleus of a HeLa cell. After photoconversion of PP2Cγ-Phamret in a region of the nucleus, we acquired fluorescence images at 41 Hz that show how fast the photoconverted PP2Cγ-Phamret diffuses (**Fig. 3** and **Supplementary Video 3** online).

### Determination of biomolecule diffusion coefficients

To determine diffusion coefficients of proteins tagged with photosensitive fluorescent proteins, we devised a new microscopy technique that enables measurement of a wide range of diffusion coefficients. This technique, FDAP, is based on measurement of fluorescence decay after photostimulation of photosensitive fluorescent proteins by quick (0.25 ms) photo-irradiation using a focused laser followed by repeated reciprocal line scanning at 4,100 Hz. We used a laser confocal microscope equipped with a dual laser scanner to carry out photostimulation during fluorescence measurement. We used Phamret as the photosensitive fluorescent protein, and measured the diffusion coefficient in aqueous solution (**Fig. 4a**). When we used averaged fluorescence decay data derived from 10 measurements directly for fitting by Eq. 3, the estimated diffusion coefficient was 70.4 ± 0.8 μm²/s. This value is much larger than 50.4 μm²/s determined by FCS for the GFP tandem dimer[23]. Because the FDAP experiment required about ten times more intense laser irradiation for excitation than that used in FRAP to acquire line images with a high-enough signal-to-noise ratio, we speculated that the difference in measured diffusion coefficients was due to photobleaching of PA-GFP moiety in Phamret during the fluorescence decay measurement (**Supplementary Fig. 3a**). To estimate the influence from photobleaching, we recorded a time course of fluorescence intensity using fully photoconverted Phamret in solution or in a cell in which we neglected the fluorescence decay caused by the molecular diffusion. Although the fluorescence attenuation rate in FDAP was larger than that expected from simple bleaching immediately after starting the measurement, the total number of bleached molecules was comparable between FDAP and FRAP at the end of measurements (**Supplementary Fig. 4a,b** online). We used the measured decay curve (**Fig. 4a**) for data compensation and applied the compensated data for nonlinear curve fitting (**Fig. 4b**). The diffusion coefficient after correction was 49.5 ± 0.6 μm²/s, which was almost equivalent to the previous FCS data[23]. Recently, a method to measure faster diffusion using FRAP by attempting to account for the finite time of the photobleaching has been proposed[24]. Therefore, we performed FRAP measurements to compare the results with those of FDAP (**Supplementary Fig. 4c–f**) and FCS analyses. All three methods gave comparable results for tandem fluorescent protein dimers (**Table 2**). However, the diffusion coefficient of a single fluorescent protein measured by FRAP was substantially different from those obtained by FDAP and FCS, indicating that FDAP may be more reliable than FRAP for analysis of fast-diffusing molecules with >20 μm²/s diffusion coefficient, provided that an accurate bleaching curve can be obtained for correction of the FDAP data (**Table 2**).

To validate the performance of FDAP, we compared the diffusion coefficient of Phamret in HeLa cells at different stages of the cell cycle (S/G2, M, early G1 and mid-G1) as well as in different compartments, cytoplasm and nucleus (**Fig. 4c**). We obtained a correction curve for this experiment using fully photoconverted Phamret in HeLa cells. Generally, the diffusion coefficient of Phamret in the nucleus was greater than that in cytoplasm except in early-G1 phase in which Phamret in both nucleus and cytoplasm showed a similar diffusion coefficient (**Fig. 4d**). Furthermore, we found that the diffusion coefficients in the nucleus during early-G1 phase (13.4 ± 3.3 μm²/s) were significantly smaller than those in other phases (17.0 ± 3.1 in S phase, 17.1 ± 2.2 in M phase, 16.8 ± 3.7 in mid-G1 phase; **Fig. 4d**). Although the cells in M phase are classified into neither cytoplasm nor nucleus because both compartments are mixed after disappearance of the nuclear membrane, the diffusion coefficient of Phamret in M phase tends to show the

**Table 2** | Comparison of FDAP with other methods

| Fluorescent protein | FDAP D (μm²/s) | FRAP D (μm²/s) | FCS D (μm²/s) |
|---|---|---|---|
| Single | 22.9 ± 3.7 | 34.0 ± 8.5 | 23.4 ± 2.5 |
| Tandem dimer | 14.1 ± 2.4 | 18.3 ± 6.4 | 16.4 ± 0.8 |

value for S and mid-G1 phase nucleus, suggesting that the cellular environment of the M-phase cell was more nuclear-like than cytoplasm-like.

## DISCUSSION

The microscopy method we developed, FDAP, allowed reliable measurement of diffusion coefficients up to ~100 μm²/s, the measurement of which has been quite difficult using FRAP. The reason why FRAP gave a different diffusion coefficient in the comparison of FDAP and FCS, may be due to the use of the first frame image after photobleaching to calculate the bleaching constant in FRAP[24]. The first frame image after photobleaching contains irrelevant diffusion data obtained during the photobleaching and the first image acquisition. Thus, this may affect the calculation of the bleaching constant, especially for fast-diffusing molecules, resulting in an overestimation of the diffusion coefficient. According to reference 25, the total bleaching time should be at least 15 times smaller than the characteristic recovery time[25]. The photostimulation time of 0.25 ms in our FDAP measurement is brief enough that the diffusion during photostimulation can be neglected. Moreover, the FRAP measurement has other drawbacks: the bleaching constant needs to be determined whenever the target molecules or intracellular environment are changed because the value of the bleaching constant depends on the diffusion constant of the target molecules. In the presence of a highly immobile fraction, the bleaching profile in the first image contains contributions of both the diffusing mobile fraction and the stationary immobile fraction, requiring complex assumptions[24]. Our FDAP method is not affected by this issue.

Compared to FCS, FDAP has the advantage of retrieving additional information regarding the states of the immobile molecules. FDAP can be used to investigate any diffusion kinetics ranging from <0.1 μm²/s to ~100 μm²/s. Notably, when compared with FCS, measurement time for a fast diffusible protein (>10 μm²/s) by FDAP is much shorter (200 ms for FDAP versus >10 s FCS[23]), which is an advantage when analyzing molecules that quickly change diffusion coefficient upon stimulation.

In the post genomic era, many cascade maps for signal transduction pathways activated by biological events have been described. These maps are very useful for understanding the mechanisms of cellular activity at the molecular level. Information on protein and molecule movement rates within cells provides enhanced understanding of not only signal transduction but also various physiological phenomena at the molecular level. The ability to measure molecular mobility over a broad kinetic range with this single technique provides a useful complement to FRAP or FCS, thus benefiting studies on molecular dynamics in living cells.

## METHODS

**Imaging.** For cell imaging we used an Olympus confocal inverted microscope FV1000 equipped with UPLSAPO 60× 1.35 numerical aperture (NA) oil objective and multi-Argon ion laser. We used a 405 nm laser diode for photostimulation. We acquired the cyan and green fluorescence signals by excitation at 458 nm and detected them at 465–510 nm and 510–600 nm wavelength range, respectively. For td-Dendra imaging, we simultaneously acquired the green (495–525 nm) and red fluorescence (560–650 nm) signals by excitation at 488 nm. We created the fluorescence ratio images using AquaCosmos software (Hamamatsu Photonics).

**Determination of diffusion coefficient by FDAP.** We estimated the activation characteristics of the laser using fixed cells expressing Phamret. First, we photoconverted Phamret in a fixed cell by the pulse irradiation with a 405-nm laser for 0.25 ms, and measured fluorescence intensity. Then we photoconverted the whole region of the same cell again until the fluorescence came to equilibrium, and again measured the fluorescence intensity. We divided the fluorescence intensity of once-photoconverted Phamret at the position ($r$) from the center of the activated region by the fluorescence intensity of fully photoconverted Phamret. We fitted the divided values at different positions to the Gaussian laser profile modified from the previously published one[26] so that the center of the activation profile became the peak value of fluorescence intensity as described by following equation:

$$C(r) = 1 - \exp\left(-K\exp\left(-\frac{2r^2}{w^2}\right)\right), \quad (1)$$

where $C(r)$ is the concentration of the photoconverted Phamret, $K$ is the activation constant for the fixed cells, and $w$ is the half-width of the laser beam at $1/e^2$ intensity.

Each FDAP experiment started with image scans, followed by a 405-nm laser irradiation for 0.25 ms on a point in the scanning area. We collected a series of line scanned images of the fluorescence emission in the region of 510–600 nm at 0.244 ms intervals (≈4,100 Hz) for 200 ms using 488-nm laser as excitation light. We skipped the first line scanning image to avoid direct influence of the irradiated pulse of the 405 nm laser. We fixed the length of line scanning to 80 pixels, and each pixel width was 103 nm. We used the central 8 pixels (0.824 μm) in the scanned line as a region of interest for the fluorescence intensity measurement. We calculated the background signals as the average intensity in the region of interest, which we measured 50 ms before photoconversion. We calculated the average fluorescence in the region of interest (ROI) at time $t$ after the photoconversion, $I_{ROI}(t)$, from each line image with the subtracted background signal. The fluorescence signal measured in a region of interest normalized to the change in total fluorescence was determined as

$$I_{rel.\ image}(t) = \frac{I_{ROI}(t)}{I_{max}}, \quad (2)$$

where $I_{max}$ is the maximum intensity after the photoconversion.

Because the measured fluorescence decay contains contribution from photobleaching, the original fluorescence decay data must be compensated. To do this, we measured a time course of the photobleaching of completely photoconverted Phamret. We then divided the originally acquired decay curve by the photobleaching curve and used the recalculated data for the curve fitting. Using the values of $K$ and $w$, we fitted the FDAP decay curves of $I_{rel.\ image^*}(t)$ to the decay function, $I_{rel.\ calc.}(t)$ modified from that reported for FRAP[27]:

$$I_{rel.\ image^*}(t) = \alpha \times I_{rel.\ calc}(t)$$
$$= \alpha\left(1 - (1-\beta)\sum_{n=0}^{+\infty}\frac{(-K)^n}{n!}\left(1 + n\left(1 + \frac{2t}{\tau_D}\right)\right)^{-1} + \beta\frac{1-e^{-K}}{K}\right) \quad (3)$$

where α is a parameter to conform $I_{rel.\ calc.}$ to $I_{rel.\ image^*}$ at $t = 0$ and $\beta$ is the fraction of immobile molecules (ranging from 0 to 1).

$\tau_D$ is the characteristic diffusion time related to the diffusion coefficient, D, by $\tau_D = w^2/4D$. The series solution for the fluorescence decay was truncated after 40 terms[18], assuring that the neglected terms made an insignificant contribution. All of the curve fittings were done by using a weighted least-squares algorithm implemented in Origin (OriginLab).

**Additional methods.** The methods for plasmid construction, cell culture and transfections, protein purification, gel filtration, spectroscopy, pH titration, measurement of photoconversion quantum yield and western blotting are available in **Supplementary Methods** online.

*Note: Supplementary information is available on the Nature Methods website.*

**ACKNOWLEDGMENTS**

We thank H. Kimura and Y. Yoneda (Osaka University) for providing the cDNA encoding H2B-GFP and PP2Cγ, and fibrillalin, respectively. We also thank D. Goto and I. Kotera for helpful comments. We also thank F. Inagaki and N. Noda for help with gel filtration analysis. This work was partially supported by grants from Scientific Research on Advanced Medical Technology of the Ministry of Labor, Health and Welfare of Japan, Precursory Research for Embryonic Science and Technology of the Japan Science and Technology Agency, and the Japanese Ministry of Education, Science and Technology.

**AUTHOR CONTRIBUTIONS**

T.M. performed experiments, analyzed data and prepared the manuscript; A.M. contributed to data analysis; T.N. contributed to the conceptual development and experimental design and performed experiments, analyzed data and prepared the manuscript.

**Published online at http://www.nature.com/naturemethods/**
**Reprints and permissions information is available online at http://npg.nature.com/reprintsandpermissions**

1. Lippincott-Schwartz, J., Snapp, E. & Kenworthy, A. Studying protein dynamics in living cells. *Nat. Rev. Mol. Cell Biol.* **2**, 444–456 (2001).
2. Zhang, J., Campbell, R.E., Ting, A.Y. & Tsien, R.Y. Creating new fluorescent probes for cell biology. *Nat. Rev. Mol. Cell Biol.* **3**, 906–918 (2002).
3. Miyawaki, A. Visualization of the spatial and temporal dynamics of intracellular signaling. *Dev. Cell* **4**, 295–305 (2003).
4. Medina, M.A. & Schwille, P. Fluorescence correlation spectroscopy for the detection and study of single molecules in biology. *Bioessays* **24**, 758–764 (2002).
5. Reits, E.A. & Neefjes, J.J. From fixed to FRAP: measuring protein mobility and activity in living cells. *Nat. Cell Biol.* **3**, E145–E147 (2001).
6. White, J. & Stelzer, E. Photobleaching GFP reveals protein dynamics inside live cells. *Trends Cell Biol.* **9**, 61–65 (1999).
7. Lukyanov, K.A., Chudakov, D.M., Lukyanov, S. & Verkhusha, V.V. Innovation: Photoactivatable fluorescent proteins. *Nat. Rev. Mol. Cell Biol.* **6**, 885–891 (2005).
8. Patterson, G.H. & Lippincott-Schwartz, J. A photoactivatable GFP for selective photolabeling of proteins and cells. *Science* **297**, 1873–1877 (2002).
9. Verkhusha, V.V. & Sorkin, A. Conversion of the monomeric red fluorescent protein into a photoactivatable probe. *Chem. Biol.* **12**, 279–285 (2005).
10. Chudakov, D.M. *et al.* Kindling fluorescent proteins for precise *in vivo* photolabeling. *Nat. Biotechnol.* **21**, 191–194 (2003).
11. Ando, R., Mizuno, H. & Miyawaki, A. Regulated fast nucleocytoplasmic shuttling observed by reversible protein highlighting. *Science* **306**, 1370–1373 (2004).
12. Ando, R., Hama, H., Yamamoto-Hino, M., Mizuno, H. & Miyawaki, A. An optical marker based on the UV-induced green-to-red photoconversion of a fluorescent protein. *Proc. Natl. Acad. Sci. USA* **99**, 12651–12656 (2002).
13. Wiedenmann, J. *et al.* EosFP, a fluorescent marker protein with UV-inducible green-to-red fluorescence conversion. *Proc. Natl. Acad. Sci. USA* **101**, 15905–15910 (2004).
14. Chudakov, D.M. *et al.* Photoswitchable cyan fluorescent protein for protein tracking. *Nat. Biotechnol.* **22**, 1435–1439 (2004).
15. Tsutsui, H., Karasawa, S., Shimizu, H., Nukina, N. & Miyawaki, A. Semi-rational engineering of a coral fluorescent protein into an efficient highlighter. *EMBO Rep.* **6**, 233–238 (2005).
16. Gurskaya, N.G. *et al.* Engineering of a monomeric green-to-red photoactivatable fluorescent protein induced by blue light. *Nat. Biotechnol.* **24**, 461–465 (2006).
17. Ballestrem, C., Wehrle-Haller, B. & Imhof, B.A. Actin dynamics in living mammalian cells. *J. Cell Sci.* **111**, 1649–1658 (1998).
18. Phair, R.D. & Misteli, T. High mobility of proteins in the mammalian cell nucleus. *Nature* **404**, 604–609 (2000).
19. Llopis, J., McCaffery, J.M., Miyawaki, A., Farquhar, M.G. & Tsien, R.Y. Measurement of cytosolic, mitochondrial, and Golgi pH in single living cells with green fluorescent proteins. *Proc. Natl. Acad. Sci. USA* **95**, 6803–6808 (1998).
20. Recalcati, S., Menotti, E. & Kühn, L.C. Peroxisomal targeting of mammalian hydroxyacid oxidase 1 requires the C-terminal tripeptide SKI. *J. Cell Sci.* **114**, 1625–1629 (2001).
21. Kimura, H. & Cook, P.R. Kinetics of core histones in living human cells: little exchange of H3 and H4 and some rapid exchange of H2B. *J. Cell Biol.* **153**, 1341–1353 (2001).
22. Gerlich, D. *et al.* Global chromosome positions are transmitted through mitosis in mammalian cells. *Cell* **112**, 751–764 (2003).
23. Pack, C., Saito, K., Tamura, M. & Kinjo, M. Microenvironment and effect of energy depletion in the nucleus analyzed by mobility of multiple oligomeric EGFPs. *Biophys. J.* **91**, 3921–3936 (2006).
24. Braga, J., Desterro, J.M.P. & Carmo-Fonseca, M. Intracellular macromolecular mobility measured by fluorescence recovery after photobleaching with confocal laser scanning microscopes. *Mol. Biol. Cell* **15**, 4749–4760 (2004).
25. Meyvis, T.K., De Smedt, S.C., Van Oostveldt, P. & Demeester, J. Fluorescence recovery after photobleaching: a versatile tool for mobility and interaction measurements in pharmaceutical research. *Pharm. Res.* **16**, 1153–1162 (1999).
26. Axelrod, D., Koppel, D.E., Schlessinger, J., Elson, E. & Webb, W.W. Mobility measurement by analysis of fluorescence photobleaching recovery kinetics. *Biophys. J.* **16**, 1055–1069 (1976).
27. Calapez, A. *et al.* The intranuclear mobility of messenger RNA binding proteins is ATP dependent and temperature sensitive. *J. Cell Biol.* **59**, 795–805 (2002).
28. Shimozono, S. *et al.* Concatenation of cyan and yellow fluorescent proteins for efficient resonance energy transfer. *Biochemistry* **45**, 6267–6271 (2006).

# Cell-cycle-specific nestin expression coordinates with morphological changes in embryonic cortical neural progenitors

**Takehiko Sunabori[1,2,3], Akinori Tokunaga[1,3], Takeharu Nagai[4,5], Kazunobu Sawamoto[1,2], Masaru Okabe[6], Atsushi Miyawaki[4], Yumi Matsuzaki[1], Takaki Miyata[7] and Hideyuki Okano[1,3,*]**

[1]Department of Physiology, [2]Bridgestone Laboratory of Developmental and Regenerative Neurobiology, Keio University School of Medicine, Tokyo 160-8582, Japan
[3]Solution Oriented Research for Evolutional Science and Technology (SORST), Japan Science and Technology Agency (JST), Saitama 332-0012, Japan
[4]Laboratory for Cell Function and Dynamics, Advanced Technology Development Center, Brain Science Institute, RIKEN, Saitama 351-0198, Japan
[5]Laboratory for Nanosystems Physiology, Research Institute for Electronic Science, Hokkaido University, Hokkaido 060-0812, Japan
[6]Genome Information Research Center, Research Institute for Microbial Diseases, Osaka University, Osaka 565-0871, Japan
[7]Department of Anatomy and Cell Biology, Graduate School of Medicine, Nagoya University, Nagoya 466-8550, Japan
*Author for correspondence (e-mail: hidokano@sc.itc.keio.ac.jp)

*Accepted 24 January 2008*
*Journal of Cell Science 121, 1204-1212 Published by The Company of Biologists 2008*
*doi:10.1242/jcs.025064*

## Summary

**During brain development, neural progenitor cells extend across the thickening brain wall and undergo mitosis. To understand how these two completely different cellular events are coordinated, we focused on the transcription pattern of the nestin gene (*Nes*), which encodes an intermediate filament protein strongly expressed in neural progenitor cells. To visualize nestin expression in vivo, we generated transgenic mice that expressed a destabilized fluorescent protein under the control of *Nes* second intronic enhancer (E/nestin:dVenus). During the neurogenic stage, when the brain wall thickens markedly, we found that nestin was regulated in a cell-cycle-dependent manner. Time-lapse imaging showed that nestin gene expression was upregulated during G1-S phase, when the neural progenitor cells elongate their fibers. However, nestin expression dramatically declined in G2-M phase, when progenitor cells round up to undergo mitosis. The cell-cycle-dependent phosphorylation of an upstream regulator class III POU transcription factor (Pou3f2 or Brn2) reduced its binding activity to the nestin core enhancer element and was therefore responsible for the decreased *Nes* transcription in G2-M phase. Collectively, these findings demonstrate precisely orchestrated gene regulation that correlates with the 3D morphological changes in neural progenitor cells in vivo.**

Supplementary material available online at
http://jcs.biologists.org/cgi/content/full/121/8/1204/DC1

Key words: Intermediate filament, Phosphorylation, Radial glia, POU, SOX, Cell cycle

## Introduction

During brain development, the primordium of each brain region, initially composed purely of neural progenitor cells (Okano, 2002), thickens as newly generated neurons accumulate between the ventricle and the pia. There are marked stage-dependent changes in the morphology of the progenitor cells in the developing cerebral cortex during the time that brain-wall thickening is most prominent (Takahashi et al., 1993) (summarized in Fig. 5A). Initially, in embryonic day (E) 9 to E11 mice, progenitor cells, called neuroepithelial cells, span the cerebral wall, crossing distances of up to 100 μm. As development proceeds, the progenitor cells adopt a radially elongated morphology connected to the ventricular and pial surfaces (also called 'radial glial' cells) (Rakic, 2003). Their extended processes span 200-300 μm by E13-E14 and 400-500 μm at E15-E16.

Although newborn progenitor cells must adapt to the developmental stage-specific changes in brain wall thickness, they must also alter their morphology in a cell-cycle-dependent manner (summarized in Fig. 5B). At the beginning of G1 phase, each progenitor cell generated at the ventricular surface either lacks its pial process (Hinds and Ruffett, 1971) or is connected to the pial surface, depending on whether or not it inherited the pial process from the parent cell (Miyata et al., 2001; Noctor et al., 2001). The daughter lacking the pial process (Fig. 5B, arrowhead ii) elaborates a new one, mainly during G1 phase, and subsequently adopts a bipolar 'radial glial' morphology by the time it reaches S phase (Miyata et al., 2001; Noctor et al., 2002). The daughter that inherited the pial process (Fig. 5B, arrowhead i) must also elongate its process to span the thickening cerebral wall, and must do so within a single cell cycle (Takahashi et al., 1993). Although the elongated processes of neural progenitor cells have long been known to serve as a scaffold for migrating newborn neurons (Rakic, 1972), how their polarized and elongated morphology is established during brain development remains unclear. Here we ask, what is the 'trick' that enables a progenitor cell to undertake two completely different jobs (elaborating a process and dividing) that must be carefully coordinated?

To approach this question, we focused on the transcriptional pattern of the nestin gene (*Nes*) for two reasons. First, nestin is strongly expressed in neural progenitor cells (Hockfield and McKay, 1985). Second, *Nes* encodes an intermediate filament (IF) protein (Lendahl et al., 1990), which comprises one of the three major

cytoskeletal systems. Furthermore, a recent report showed that IFs are involved in the establishment of the bipolar morphology and also the twisting of the pial process that influences the kinetics of neural progenitor nuclear movement (Miyata and Ogawa, 2007). Moreover, several papers have shown that nestin is important in regulating the assembly or disassembly of the IF network (Sahlgren et al., 2001; Chou et al., 2003), and it has been proposed to function as a crossbridge with other cytoskeletal systems (Marvin et al., 1998). Thus, we predicted that the transcription of *Nes* might be coordinated with the stage- or cell-cycle-dependent morphological alteration of neural progenitor cells. To elucidate the mechanism for regulating *Nes* expression, we observed its transcription pattern in vivo, relative to cell development and the cell cycle.

## Results

### Expression pattern of E/nestin:dVenus transgene in the developing CNS

To evaluate accurate *Nes* expression, we needed a new tool, because the previously established transgenic mice expressed EGFP under control of the *Nes* second intronic enhancer (Kawaguchi et al., 2001). EGFP is stable for too long to be used in evaluating changes that occur within such a short period as a single cell cycle. Therefore, we generated transgenic mice expressing destabilized Venus (dVenus) under the control of the same driver – the *Nes* second intronic enhancer (E/nestin:dVenus; Fig. 1A). Venus is a GFP derivative made from YFP and contains mutations that greatly accelerate the maturation of the fluorescent protein at 37°C. It also shows 10- to 100-fold stronger fluorescence than YFP in vitro (Nagai et al., 2002). In the dVenus construct, a PEST amino acid sequence from mouse ornithine decarboxylase is fused to the C-terminus of Venus, thus targeting the protein for rapid, cell-cycle-independent intracellular degradation (Li et al., 1998; Corish and Tyler-Smith, 1999). Therefore, the dVenus reporter cassette allows the strict on-off enhancer-promoter activity to be detected as a fluorescent signal (Kohyama et al., 2005).

Four independent mouse lines showed virtually identical dVenus expression patterns, indicating that its expression profile was consistent regardless of the transgene insertion site. dVenus was first detected around E8.5 throughout the central nervous system (CNS) and the signal became much weaker by E17.5 (data not shown).

We first observed coronal sections of the developing forebrain of E/nestin:dVenus transgenic mice. The dVenus fluorescence was localized strictly to the ventricular zone (VZ) at all developmental stages (supplementary material Fig. S1). Because our focus was on the regulation of *Nes* transcription, we also studied the expression patterns of molecules from candidate regulator genes. The *cis*-element of *Nes* used to drive dVenus expression has been extensively studied, and the evolutionarily conserved region in the 3′ half of the second intron contains an enhancer that is synergistically regulated by group B1 SOXs (SOX1-SOX3) and class III POU (Pit-Oct-Unc) transcription factors (Zimmerman et al., 1994; Lothian and Lendahl, 1997; Josephson et al., 1998; Tanaka et al., 2004). We found that the expression of both transcription factors roughly paralleled that of the dVenus expression during neurogenesis (supplementary material Fig. S1).

### Usefulness of E/nestin:dVenus mice and correlation between fluorescence intensity and *Nes* mRNA expression

To confirm that the dVenus expression pattern of our novel transgenic mice faithfully reproduced the expression pattern of endogenous nestin, we first compared the dVenus expression from our transgenic mice with the EGFP pattern of E/nestin:EGFP mice, in which the EGFP sequence is driven by the same regulatory sequence as in the dVenus-expressing transgenic mice (Kawaguchi et al., 2001). To evaluate the transgenic lines under the same conditions, we mated E/nestin:dVenus with E/nestin:EGFP transgenic mice and generated a double-transgenic embryo. Because dVenus is a modified YFP, their emission spectra were close (Fig. 1B). To separate the signals from the same section, we used the linear unmixing function of the confocal laser-scanning microscope LSM510 META (Zeiss). Brains from E14.5 embryos expressing both transgenes were sectioned and counterstained with an antibody to β-tubulin III, an early neuronal marker (Fig. 1C,D). We found that the dVenus-expressing cells were entirely included within the population of EGFP-positive cells in the VZ, and there was no overlap between dVenus expression and β-tubulin-III-expressing neurons (Fig. 1D). However, some EGFP-positive cells were double-labeled for β-tubulin III, and the EGFP signal persisted in cells in the intermediate zone, even after their neuronal differentiation (Fig. 1D, arrowheads). These results indicated that the E/nestin:dVenus transgenic mice expressed dVenus only in cells that had not differentiated into neurons, showing that the dVenus fluorescence was more faithful to the nestin expression pattern than the EGFP fluorescence driven by the same enhancer.

To determine the correlation between dVenus expression and the differentiation state, we sorted cerebral wall cells from dVenus transgenic embryos by fluorescence-activated cell sorting (FACS). Cells were fractionated into dVenus-positive (F2) and -negative (F1) populations, following the profile of the negative control from wild-type mouse brain (Fig. 1E). We characterized the cells in each fraction using antibodies against nestin and β-tubulin III. As expected, nestin-expressing cells were abundant (96.4±1.2%) in the F2 fraction, and made up less (26.9±1.0%) of the F1 fraction. The relative abundance of the β-tubulin-III-positive cells was reciprocal to that of the nestin-expressing cells: they made up 0.7±1.0% of the cells in F2 and 80.3±6.4% of the cells in F1 (Fig. 1F).

To confirm the accuracy of the sorting process, we also used an anti-GFP antibody to label dVenus. We found that the dVenus-expressing cells were reliably sorted into the F2 fraction (94.7±2.5%) and were almost absent from the F1 fraction (1.0±0.3%) (Fig. 1F). Moreover, cells from the F2 fraction formed self-renewable and multipotent neurospheres at a much higher rate (16±1 cells/500 cells) than those from the F1 fraction (0.2±0.4 cells/500 cells) (supplementary material Fig. S2B,C). These observations confirmed that our new dVenus reporter transgenic mice were more useful than the E/nestin:EGFP transgenic mice for characterizing neural stem/progenitor cells.

To determine the correlation between *Nes* mRNA expression and dVenus fluorescence intensity, we subdivided the dVenus-positive fraction (F2) into equal subfractions containing the high (F4) and low (F3) transgene-expressing-cells, based on fluorescence intensity (Fig. 1E). The level of *Nes* mRNA in the dVenus (and largely nestin)-positive progenitor populations (F3 and F4) and the dVenus-negative fraction (F1) was determined by real-time quantitative PCR. The fluorescence intensity of the E/nestin:dVenus cells exhibited a positive correlation with the amount of *Nes* mRNA (Fig. 1G), indicating that the reporter expression reflects the actual expression of *Nes* mRNA. Therefore, we monitored the expression level of *Nes* mRNA via the fluorescence intensity of dVenus in vivo.

### Cell cycle-dependent expression of *Nes* mRNA

Because EGFP is a stable protein, the level of fluorescence produced by E/nestin:EGFP was uniform throughout the embryonic VZ. By contrast, owing to the short half-life of dVenus, the fluorescence in the VZ of E/nestin:dVenus embryos showed scattered fluorescent cells (Fig. 1D). This observation was consistent with our idea that the enhancer activity of *Nes* might be regulated by the cell cycle in neural progenitors, particularly because the VZ contains proliferating cells in various cell cycle phases. Therefore, we focused on the relationship between dVenus expression and the cell cycle.

Each cell cycle phase was discriminated by labeling the cells for differing periods of time before sacrifice with thymidine analogues (Fig. 2A; see Materials and Methods for details). The cells that expressed dVenus were counted at each cell cycle phase. To label cells in S phase, IdU was injected into pregnant dams 30 minutes before sacrifice (Fig. 2B purple). A high proportion of cells in S phase expressed dVenus (Fig. 2B arrowheads; 63.3±5.2%). However, cells in G2-M phase, which were labeled by injecting IdU 3 hours before sacrifice (Fig. 2C red), showed hardly any dVenus expression (Fig. 2C arrows; 9.3±1.4%). dVenus expression was stronger (Fig. 2D arrowheads; 47.4±7.9%) in G1 phase cells, which were labeled by injecting IdU 14.5 hours before sacrifice (Fig. 2D red). To distinguish cells in S phase, BrdU was injected 30 minutes before sacrifice in all trials (Fig. 2B-D purple). These data strongly support the hypothesis that *Nes* expression is regulated in a cell-cycle-dependent manner within the VZ, with expression being downregulated during G2-M phase (Fig. 2E).

### *Nes* is strongly expressed in radially elongating G1-phase VZ cells and is downregulated in G2-M phase

Cortical progenitor cells positive for nestin protein show dynamic morphological changes in vivo (summarized in Fig. 5). Because pharmacological depolymerization of IFs by calyculin-A affects the bipolar morphology of neural progenitor cells in vivo (Miyata and Ogawa, 2007), we next explored the relationship between *Nes* expression and the three-dimensional (3D) morphology of the neural progenitor cells, especially the radial glial cells. To visualize live radial glial cells, we placed DiI on the pial surface of the cerebrum and performed time-lapse imaging of cerebral wall slices. Radial glial cells are known to retain the radial process during mitosis, and the fiber is inherited by one of the daughter cells (Miyata et al., 2001; Noctor et al., 2001). Fig. 3A shows a series of time-lapse imaging of a pair of daughter cells 4 hours after their birth at the ventricular surface. The daughter cell that did not inherit the radial fiber (Fig. 3A, arrowhead ii) began to extend a new pial process, and its sister cell (Fig. 3A, arrowhead i) thickened and extended its inherited fiber 20 μm according to the brain wall thickening within this period (Fig. 3A, *). The strong expression of dVenus observed in both of the newly born daughter cells (Fig. 3A) confirmed that the expression level increased during G1 phase, as we had observed in the BrdU/IdU labeling assay (Fig. 2). This observation also demonstrated that the dynamic activation of the *Nes* enhancer correlates with the 3D growth of cortical progenitor cells.

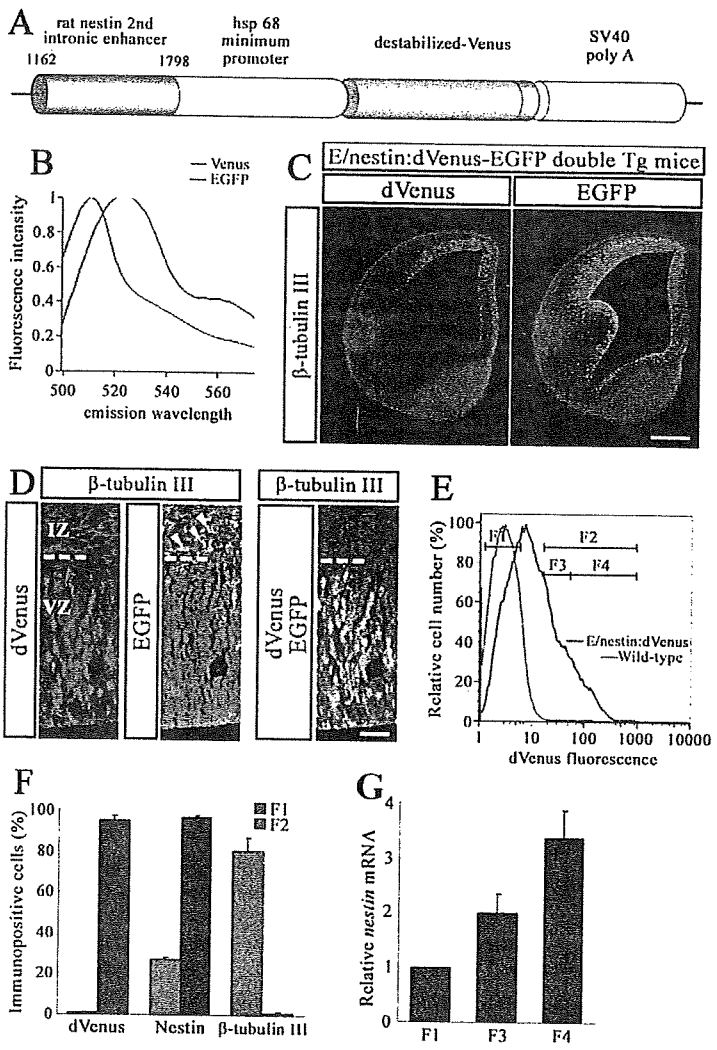


**Fig. 1.** E/nestin:dVenus fluorescence intensity is correlated with *Nes* mRNA expression. (A) Structure of the E/nestin:dVenus transgene. (B) Emission spectra of Venus (green) and EGFP (red). (C,D) On an identical section from an E14 E/nestin:dVenus-EGFP double transgenic embryo, no dVenus-expressing cells showed immunoreactivity against the anti-β-tubulin III antibody, although some EGFP-expressing cells did (arrowheads). VZ, ventricular zone; IZ, intermediate zone. (E) Representative FACS profile of cerebral-wall-derived cells from an E14.5 E/nestin:dVenus transgenic embryo. (F) Quantitative data showing the percentage of E/nestin:dVenus negative (F1) and positive (F2) cells immunostained with nestin, β-tubulin III and GFP antibodies. (G) To compare the E/nestin:dVenus fluorescence intensity with the *Nes* mRNA expression level, real-time quantitative PCR was performed. dVenus-positive cells were subdivided into two fractions based on their fluorescence intensity: high (F4) and low (F3). The *Nes* mRNA expression level of these two fractions (F4 and F3), as well as of the dVenus-negative cells (F1), showed a positive correlation with the fluorescence intensity. Data are means ± s.e.m. Scale bars: 500 μm (C), 25 μm (D).

Because the nuclear movement towards the ventricular surface (adventricular migration) is characteristic of G2 phase progenitor cells (Hayes and Nowakowski, 2000), we next asked whether progenitor cells whose nucleus was translocating toward the ventricular surface would show downregulated dVenus expression, as the BrdU/IdU labeling suggested (Fig. 2). As expected, dVenus was consistently undetectable in these G2-phase cells (Fig. 3B)

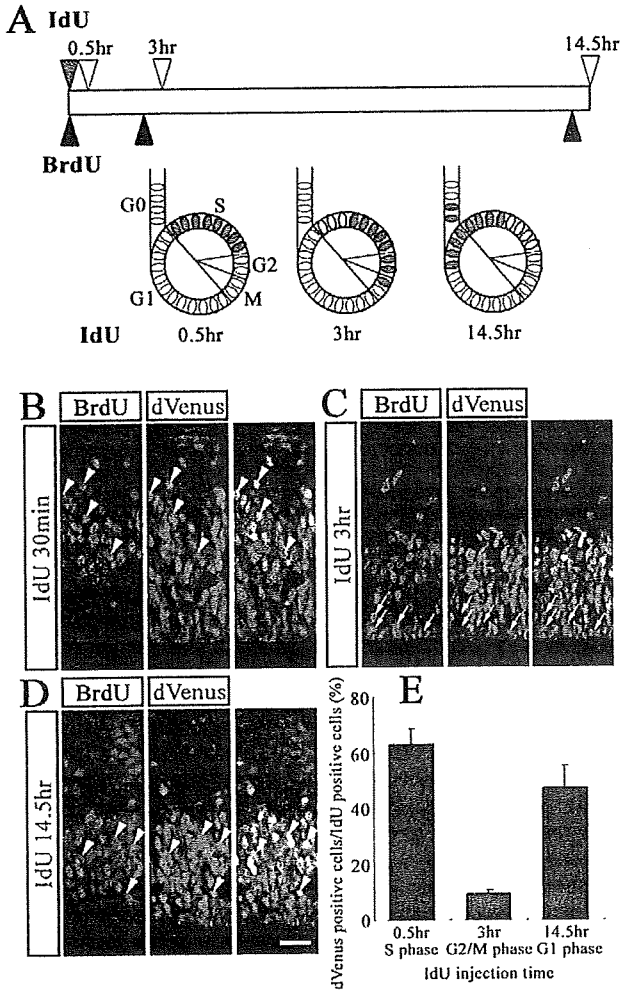


**Fig. 2.** Cell-cycle-dependent expression of *Nes*. (A) Schematic diagram of the timing used to administer thymidine analogues to label cells in each cell-cycle phase (see Materials and Methods for details). (B-D) IdU (red) was injected for 0.5 hour (B), 3 hours (C) and 14.5 hours (D) to label cells in S, G2-M and G1 phases, respectively. BrdU (purple) was injected 30 minutes before sacrifice to label cells in S phase. dVenus (green) was expressed in many of the cells in G1 and S phase (arrowheads), but cells in the G2-M phase were mostly dVenus negative (arrows). (E) Ratio of IdU-positive cells that expressed dVenus to the total number of IdU-positive cells, counted for each cell-cycle phase. Cells in G1 and S phase expressed the highest levels of dVenus, whereas its expression levels were much lower during G2-M phase. Scale bar: 25 μm (B-D). Data represent the mean ± s.e.m.

($n$=4). Immunostaining for phospho-histone H3 further demonstrated the lack of dVenus expression in M-phase cells (Fig. 3C). Thus, *Nes* expression is high in G1 phase during process extension, and it is lost in G2-M phase, which is characterized by the adventricular nuclear movement and rounding up of the soma.

### Phosphorylation of Brn2 on Ser362 reduces Brn2 binding to DNA and lowers the expression of *Nes* during G2-M

We next addressed the underlying molecular mechanism of the cell-cycle-dependent regulation of *Nes*. We first investigated whether the responsible transcription factors were expressed in a cell-cycle-dependent manner. Immunohistochemical analysis for SOX1-SOX3 and class III POU transcription factor (Pou3f2 or Brn2) showed them to be expressed ubiquitously throughout the VZ (Fig. 4A), indicating that dVenus was expressed only in a subset of these SOX- or POU-expressing cells. This result led us to consider whether post-translational modification of the transcription factors might contribute to the cyclic changes in dVenus expression.

Phosphorylation inhibits the DNA-binding activity of POU proteins such as Oct1 and GHF1 (Pit1) during G2-M (Kapiloff et al., 1991; Segil et al., 1991; Caelles et al., 1995), and the phospho-acceptor site is highly conserved in all POU-domain proteins. This site corresponds to Ser362 in Brn2. Therefore, we next asked whether the phosphorylation of Brn2 increased during G2-M in vitro. 293T cells expressing Flag-tagged Brn2 or Brn2 S362A, in which Ser362 is replaced by alanine, were synchronized at G1, S and G2-M phases (supplementary material Fig. S3), and labeled with [$^{32}$P]orthophosphate (GE Healthcare) for the 6 hours preceding harvest. The level of Brn2 phosphorylation was low in G1 (Fig. 4B lane 1) and S (Fig. 4B lane 2) phases, but it increased as the cells progressed through the cycle to G2-M phase (Fig. 4B lane 3). By contrast, the phosphorylation level of Brn2 S362A remained constant, showing essentially the same level in G2-M (Fig. 4B lane 5) as in G1 (Fig. 4B lane 4). These results indicate that Brn2 is phosphorylated on Ser362, in a cell-cycle-dependent manner, during G2-M phase.

To investigate the relationship between the phosphorylation of Brn2 and *Nes* expression, we next introduced a phosphorylation-mimicking point mutation that substituted Asp for Ser at Brn2 Ser362. We first used this construct in luciferase reporter assays (Fig. 4C). An octamerized 30-mer nestin core enhancer (Nes30) (Tanaka et al., 2004), which includes the SOX- and POU-binding sites, was fused to the rabbit β-globin minimal promoter and inserted into the pGL3 basic luciferase reporter vector. When SOX2 was expressed alone, Nes30 was weakly activated (4.5-fold). The expression of Brn2 alone led to stronger activation (8.6-fold). By contrast, Brn2 S362D increased reporter expression only slightly, to twice the basal level. When SOX2 and Brn2 were expressed together, Nes30 activity increased dramatically (24.5-fold). This synergistic action, consistent with a previous report (Tanaka et al., 2004), remarkably reduces when Brn2 was replaced with Brn2 S362D in the same experiment. The Nes30 activity increase (5-fold) was the same as for SOX2 alone (Fig. 4C).

This effect of expressing phospho-mimicking Brn2 on Nes30 activity could be caused by a decreased binding affinity for DNA or by instability of the phosphorylated Brn2. We performed an electrophoretic mobility shift assay (EMSA) to discriminate between these possibilities, using the Nes30 sequence probe and whole-cell lysates of 293T cells overexpressing Flag-tagged Brn2 or Brn2 S362D. The amount of Brn2 S362D binding complex was significantly reduced (Fig. 4D black arrow; lane 3), compared with that of wild-type Brn2 (Fig. 4D black arrow; lane 2). To ascertain whether the binding to Nes30 was Brn2 specific, an anti-Flag antibody was added to the binding reactions in a super-shift assay, which showed specific binding of the Flag-tagged Brn2 (Fig. 4D black arrowhead; lanes 4, 5). No binding reaction was observed in lysates of untransfected 293T cells (Fig. 4D lane 1), and no significant difference was seen between the stability of Brn2 and phospho-mimicking Brn2 S362D (Fig. 4E lane 2, 3), normalized to the expression of α-tubulin (Fig. 4E, *), consistent with the uniform expression pattern of Brn2 in the VZ in vivo (Fig. 4A). These results strongly suggested that the reduction of *Nes* expression

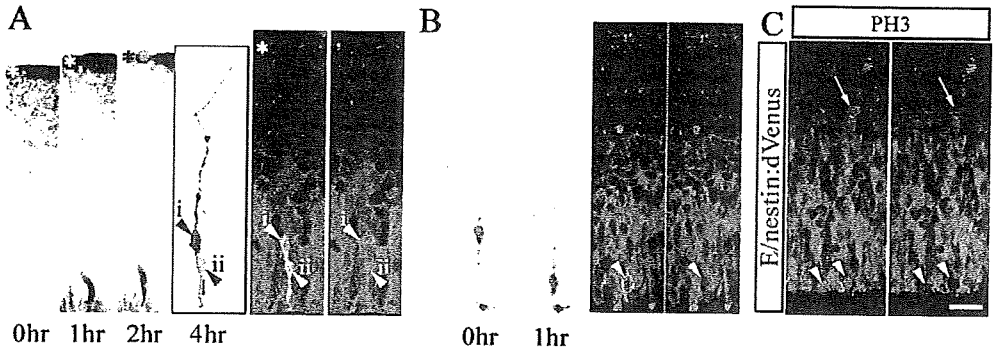


**Fig. 3.** The relationship between *Nes* expression levels and the 3D morphology of neural progenitor cells. (A) VZ cells were labeled with DiI (red) from the pial surface and observed for 4 hours after mitosis. The radial fiber, which became extremely thin during mitosis, was inherited by one of the daughter cells (arrowhead i). Four hours after mitosis, both daughter cells expressed dVenus. Within this period, the cell that inherited the process thickened its fiber and extended 20 μm (arrowhead i), whereas the cell that did not inherit the fiber began to elaborate its own process (arrowhead ii). (B) During G2 phase, the VZ progenitor cells possessed a mature fiber, and each nucleus migrated toward the ventricular surface. dVenus was not expressed in the cells during this phase (arrowhead). (C) Cells in M phase, labeled with phospho-histone H3 (PH3), were dVenus-negative both near the ventricular surface (arrowheads) and in the subventricular zone (arrow). The asterisk indicates the pial surface. Scale bar: 25 μm (A-C).

during G2-M phase is due to the decreased binding affinity of phosphorylated Brn2 for the *Nes* core enhancer element. Therefore, we conclude that the phosphorylation of POU transcription factors downregulates the cell-cycle-dependent expression of *Nes*.

## Discussion

### E/nestin:dVenus transgenic mice as a versatile model system

GFP and its variants are widely used as reporters for gene expression, lineage tracing and protein localization studies. The stability of GFP allows its accumulation and enables it to be detected easily in living cells. However, this stability also limits its application in studies requiring rapid reporter turnover. The transgenic mice reported here, which express a fluorescent reporter with a short half-life, showed the strict localization of dVenus to the VZ, which contains neural progenitors (Fig. 1C), and its expression pattern was mutually exclusive with that of an early neuronal marker, β-tubulin III (Fig. 1D). In transgenic mice carrying an EGFP reporter under the same regulatory sequence (Kawaguchi et al., 2001), the fluorescent signal was still detectable after cells had differentiated into neurons (Fig. 1D). Therefore, the novel transgenic mouse expressed dVenus in the desired pattern, but with a half-life that restricted its expression to neural progenitors. Our novel transgenic mice also allowed us to prospectively isolate self-renewable and multipotent neural stem cells using flow cytometry (supplementary material Fig. S2), and real-time quantitative PCR analysis showed that the dVenus reporter fluorescence intensity accurately reflected the relative expression levels of *Nes* mRNA (Fig. 1G). These results confirmed the utility of this reporter system. We then used this system to trace changes in the transcription of *Nes* in vivo during the cell cycle.

### Relationship between SOX-POU signaling and the maintenance of neural progenitor cells

The SOX family of HMG-box transcription factors is a key regulator of embryonic development and cell-fate determination. In certain cases, SOX1-SOX3 interact with various partner transcription factors and participate in defining distinct cell states that depend on the partner factors, such as Pax6 in lens differentiation, Oct3/4 in establishing the epiblast/ES cell state and Brn2 in the neural primordium (Kamachi et al., 2000; Tanaka et al., 2004). Although SOX1-SOX3 are known to suppress neurogenesis by maintaining neural progenitor cells in an undifferentiated state in the vertebrate CNS (Bylund et al., 2003), the responsible target gene has not been identified. Since *Nes* is a target gene of SOX and POU transcription factors (Tanaka et al., 2004), we monitored its expression pattern to learn more about the contribution of SOX proteins to the maintenance of the neural progenitor cell state. We found that the expression of *Nes*, as represented by the fluorescence intensity of dVenus, reflected its activation by a SOX-POU complex (supplementary material Fig. S1). We also found that transcription by the SOX-POU complex was inactivated during G2-M (Figs 2, 3) by the cell-cycle-dependent phosphorylation of the POU transcription factor (Fig. 4). Our data suggest that the cell-fate choice to remain an undifferentiated neural progenitor cell, regulated by the SOX-POU complex, is completed during G1 to S phase. Interestingly, the activation of Notch1 (indicated by its nuclear localization), which maintains neural progenitor cells in the undifferentiated state by inducing Hes1/5 expression (Gaiano and Fishell, 2002), also takes place in G1 to S phase (Tokunaga et al., 2004). However, it is still unclear whether cells that have been stimulated with SOX-POU during the early G1 phase can change their cell fate decision and differentiate into neurons without further progression of the cell cycle. Therefore, future research needs to address the timing of the cell-fate decision during G1 phase of daughter cells. Our present study demonstrates that the target genes of the SOX-POU transcription factor complex are regulated in a more complicated manner than expected (Tanaka et al., 2004), and it provides a model for further understanding the contribution of SOX transcription factors to the maintenance of neural progenitor cells in an undifferentiated state.

### Cell-cycle-dependent expression of nestin

By allowing mouse cells to incorporate thymidine analogues at different times before sacrifice, we confirmed that *Nes* expression was regulated in a cell-cycle-dependent manner in vivo (Fig. 2). Moreover, in vitro experiments suggested that the weak *Nes* expression during G2-M could be attributed to the cell-cycle-dependent phosphorylation of Brn2 (Fig. 4B). This phosphoacceptor

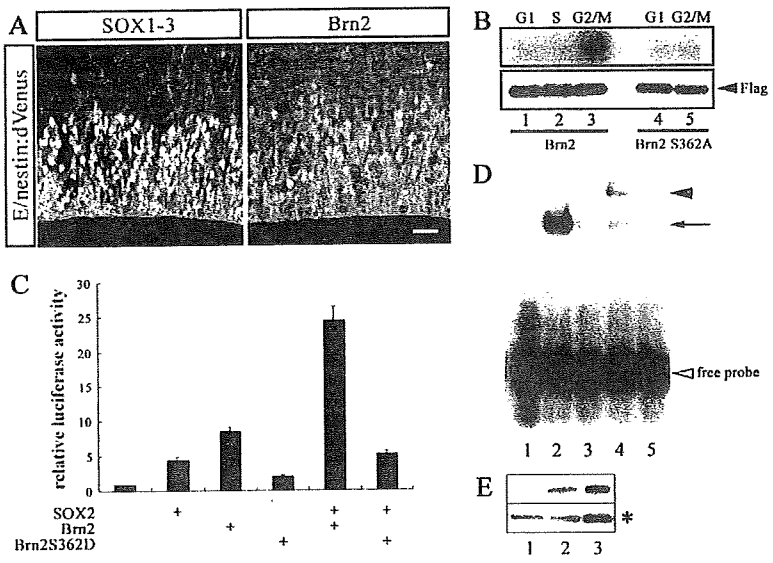


**Fig. 4.** The expression of *Nes* is reduced by the decreased affinity of Brn2 phosphorylated on Ser362 for the *Nes* core enhancer during G2-M. (A) Immunostaining showed that only a subset of SOX1-SOX3 and Brn2 immunopositive cells expressed dVenus in the E14.5 cerebral cortex. (B) Flag-tagged Brn2- and Brn2-S362A-expressing 293T cells were synchronized at the G1, S and G2-M phases and labeled with [$^{32}$P]orthophosphate. The low level of Brn2 phosphorylation at G1 and S (lane 1, 2) increased during the G2-M phase (lane 3). However, the phosphorylation level of Brn2 S362A at G2-M (lane 5) was the same as in the G1 phase (lane 4). (C) SOX2, Brn2 and Brn2 S362D were used to transfect cells either alone, or as a SOX-POU combination, with a luciferase-encoding reporter plasmid carrying an octamerized nestin core enhancer sequence (8×Nes30). Together, SOX2 and Brn2 synergistically activated the 8×Nes30 reporter. By contrast, when Brn2 was replaced with Brn2 S362D, the activation was markedly lower. Data represent means ± s.e.m. (D) EMSA showing the lower binding affinity of Brn2 S362D (lane 3) compared with the wild-type Brn2 (lane 2) for the Nes30 probe (black arrow). The binding specificity was confirmed by a super shift assay (black arrowhead; lanes 4, 5). No binding reaction was seen with the lysate of untransfected 293T cells (lane 1). Open arrowhead indicates the free probe. (E) Western blot showing the Brn2 and Brn2 S362D input used for the EMSA. No significant difference was seen between the stability of Brn2 and Brn2 S362D when normalized to α-tubulin expression (*). Scale bar: 25 μm.

site at Brn2 Ser362 is highly conserved in all POU-domain proteins, and other POU proteins, such as Oct1 and GHF1 (Pit1), are phosphorylated on the same site during G2-M (Kapiloff et al., 1991; Segil et al., 1991; Caelles et al., 1995). In agreement, our data showed a marked decrease in reporter activity from the *Nes* core enhancer when Asp was substituted for Brn2 Ser362 (Fig. 4C). By EMSA, we demonstrated that the reduced transcription was due to a dramatic drop in Brn2 S362D binding of the *Nes* core enhancer, compared with wild-type Brn2 (Fig. 4D). Our hypothesis that cell-cycle-dependent Brn2 phosphorylation regulates *Nes* expression is based on in vitro studies, and we have not characterized the kinase responsible for this regulation. However, because Cdc2 mitotic kinase, which is ubiquitously expressed in all cells during G2-M phase, is a candidate kinase for the cell-cycle-dependent phosphorylation of Oct1 and GHF1 (Segil et al., 1991; Caelles et al., 1995), it is reasonable to expect that Brn2 is subject to the same regulatory mechanism in the developing brain in vivo.

### Physiological relevance of nestin in neural progenitor cells in vivo

In spite of the numerous IF family members, the expression of IFs exhibits a high degree of cell-type specificity (Herrmann and Aebi, 2004). The unique physical properties and interaction capabilities of these distinct IF molecules with accessory proteins mediate the generation of a highly dynamic and interconnected cell-type-specific cytoarchitecture. In the CNS, undifferentiated progenitor cells express nestin and vimentin. During neural differentiation, nestin is downregulated and displaced with the expression of neurofilament (NF) proteins and/or peripherin in neurons, and GFAP in astrocytes (Lariviere and Julien, 2003). Although many of the gene-targeting approaches of the neural IF genes demonstrate mild phenotypes, substantial developmental loss of motor axons was detected in mice lacking NF-L and in NF-M–NF-H double knockout mice. Mice lacking NF-L also had a scarcity of IF structures and exhibited a severe axonal hypotrophy (Lariviere and Julien, 2003). In GFAP and vimentin double-deficient mice, the post-traumatic glial scarring was looser and less organized (Pekny et al., 1999). This evidence supports a role for IFs in cytogenesis and stabilization.

Nestin cannot form filaments of its own, but it can readily form copolymer IFs when combined with vimentin both in vivo and in vitro (Marvin et al., 1998; Steinert et al., 1999). A complex of nestin-vimentin heterodimers is less stable than vimentin homopolymers when subjected to increasing concentrations of urea in vitro (Steinert et al., 1999). Therefore, nestin can retain the flexibility of the IF network in neural progenitor cells. It has been reported that the pial process of neural progenitor cells exhibits a coiled or hairpin-loop structure that produces a spring-like force, which functions to propel the cell soma away from the proliferating VZ (Miyata and Ogawa, 2007). Since the IF network has been shown to have a vital role for this twisting of the process (Miyata and Ogawa, 2007), nestin can enable the neural progenitor cell to possess this complicated architecture. This assumption is supported by the fact that the IF network depolymerizes during M phase, requiring the twisting process to take place during G1 phase when the *Nes* transcription is most prominent (Fig. 2).

Furthermore, nestin has been reported as a potential target of cyclin-dependent kinase 5 (Cdk5) and phosphorylation may target it for subsequent ubiquitylation and degradation outside the VZ (Sahlgren et al., 2003). In the Cdk5-deficient cortex, nestin expression persisted in cortical neurons (Cicero and Herrup, 2005), suggesting that the post-translational modification fine-tunes the expression of nestin. Since Cdk5 is predominantly observed outside the VZ, phosphorylation of nestin must take place after the transcriptional shutdown (Fig. 1D). Interestingly, transcription of *Nes* is also downregulated in G2-M (Fig. 2) when Cdc2 phosphorylates nestin (Sahlgren et al., 2001; Chou et al., 2003), suggesting that the transcription and post-translational modification is precisely orchestrated.

### Correlation between *Nes* expression and morphological change in neural progenitor cells in vivo

The reduction in the binding activity of transcription factors during G2-M might be a general event that frees chromatin during mitosis.

However, we also found that the molecular regulation of *Nes* correlated with changes in the 3D morphology of the neural progenitor cell in vivo. During the transition from M to G1, the process of the progenitor cell becomes extremely thin. Simultaneously, mitosis-specific phosphorylation promotes disassembly of the IF network (Yasui et al., 2001; Sahlgren et al., 2001; Noctor et al., 2002; Chou et al., 2003). Although the thin fiber is retained during M phase and inherited by only one of the daughter cells (Fig. 3A), both daughter cells must reorganize their cytoskeleton during G1 to S phase, either to extend a new process or to thicken the inherited one and elongate it to match the increasing width of the cerebral wall. Even if the nestin protein is stable and is divided equally between the daughter cells, it must double in quantity to effect this network-remodeling step. In addition, this cyclical regulation of *Nes* transcription provides nestin concomitant with the elongation of the radial fiber in G1 to S phase (Fig. 2 and Fig. 3A), which must happen at each division because of the continuous thickening of the cerebral wall (Takahashi et al., 1993). Moreover, it is interesting that the length of G1 phase extends during development (Takahashi et al., 1995), simultaneously with the requirement for a longer process, as the cerebral wall thickens (Takahashi et al., 1993).

In addition to nestin being supplied when needed for process elongation, the dramatic decline in *Nes* expression during G2 phase, when neural progenitor cells possess a thick and matured process, is also crucial for normal morphological dynamics (Fig. 2 and Fig. 3B,C). It is known that nestin disassembles the IFs through phosphorylation during the transition from M to G1 (Sahlgren et al., 2001; Chou et al., 2003). However, an extremely high dosage of nestin can also disassemble the IFs physically (Steinert et al., 1999), irrespective of its phosphorylation state. Thus, the reduction of *Nes* transcription in G2-M phase is essential, once the progenitor cell obtains a mature IF network, for preserving the appropriate timing of IF disassembly. Furthermore, an attractive hypothesis is that the expression of *Nes* correlates with the cell-cycle-dependent migration of the nuclei, described as interkinetic nuclear movement (Sauer and Walker, 1959; Fujita, 1962). Recently, several groups proposed that microtuble- and actin-dependent mechanisms are important for the adventricular nuclear movement in G2 phase. Knockdown of LIS1 (Tsai et al., 2005), myosin II (Tsai et al., 2007), Cep120 and transforming acid coiled-coil proteins (TACCs) (Xie et al., 2007) impaired the migration of the nuclei towards the ventricular surface without affecting the bipolor morphology of the neural progenitor cell. By contrast, the mechanism of migrating away from the ventricular surface in G1 phase, which is slower than the adventricular migration (Takahashi et al., 1995), remains unknown. Because of the synchronization of *Nes* transcription and the nuclear movement, nestin could be involved not only in the extension of the progenitor cell, but also the nuclear movement in G1 phase. Building on previously reported results showing that IF depolymerization creates abnormal neural progenitor cell morphology (Miyata and Ogawa, 2007), our present study, which accurately maps the expression profile of *Nes*, strongly suggests that not only post-translational modification but also precise transcriptional regulation are vital for (1) maintaining the 3D morphology of neural progenitor cells and (2) their mitotic cycle, through remodeling of the cytoskeletal network in vivo (Fig. 5).

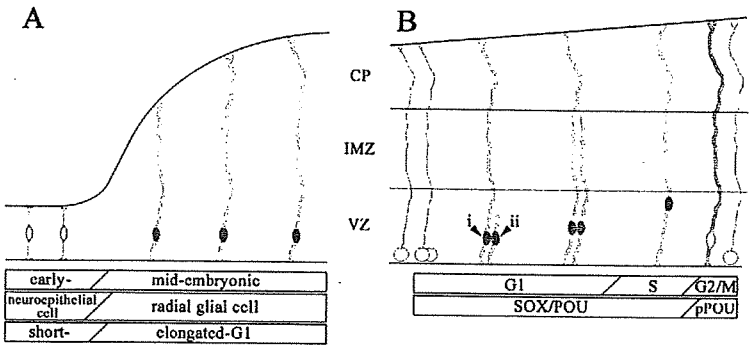


**Fig. 5.** A schematic diagram of *Nes* expression according to the cell-cycle-dependent morphological changes of neural progenitor cells in the developing cerebral cortex. (A) A schematic diagram of the stage-dependent thickening of the mouse cerebral wall based on Takahashi et al. (Takahashi et al., 1993). Cortical progenitor cells elongate as development proceeds from an early 'neuroepithelial cell' to a mid-embryonic 'radial glial cell' stage. The expression of *Nes* (green) was strong during the neurogenic stage, which accompanied obvious cerebral wall thickening and the prolonged G1 phase. (B) Cell-cycle-dependent morphological changes of mid-embryonic progenitor cells. At the beginning of the G1 phase, each progenitor cell generated at the ventricular surface is either connected to the pial surface (cell i) or lacking a pial process (cell ii). The daughter cell that inherited the pial process (cell i) elongates its process within a single cell cycle to match the cerebral wall thickening. The other daughter cell (cell ii) elaborates a new pial process, mainly during G1, and adopts the bipolar radial glial morphology by S phase. During mitosis, the cell body rounds up and the process becomes extremely thin. A model for the lineage-restriction of the progenitor cell is omitted for simplification. The expression of *Nes* (green) was observed concomitant with the elongation of the radial process during the G1 to S phases. At G2-M, *Nes* expression declined because of the phosphorylation of its upstream regulator class III POU protein, allowing the cells to undergo mitosis. Note that the duration of each cell cycle phase illustrated (G1, S, and G2-M) is according to those determined at E14 by Takahashi et al. (Takahashi et al., 1995). CP, cortical plate; IMZ, intermediate zone; VZ, ventricular zone.

## Materials and Methods

### Production of transgenic mice

The 637 bp (1162-1798) fragment of the second intronic region of rat *Nes* with the minimum promoter of heat shock protein 68 (hsp68) from the nestin-hsp68-EGFP plasmid (Kawaguchi et al., 2001) was subcloned into the *AseI-BamH*I site of pd4EGFP-N1 (BD Biosciences, San Jose, CA). The gene for Venus was inserted into this plasmid in place of that for EGFP. The purified transgene was microinjected into the pronucleus of fertilized mouse eggs. Four independent lines showing identical expression patterns were generated in a C57BL/6 background. The data presented are from experiments using heterozygous mice from a single line. All procedures were performed in accordance with institutional guidelines. The date of conception was established by the presence of a vaginal plug and recorded as E0.5.

### Immunohistochemistry and immunocytochemistry

Post-fixed mouse embryo brains were embedded in 3% LMP Agarose (Invitrogen, Carlsbad, CA) and sectioned at 50 μm on a vibratome (VT1000; Leica, Heidelberg, Germany). Free-floating sections were washed twice with 0.1 M phosphate-buffered saline, pH 7.4 (PBS) and blocked with blocking solution (PBS containing 5% normal donkey serum and 0.3% Triton X-100; Sigma-Aldrich, St Louis, MO) for 30 minutes. Subsequently, sections were incubated overnight at 4°C in a mixture of the primary antibodies described above, in blocking solution. After washing three times with PBS, sections were reacted with secondary antibodies at room temperature for 2 hours, washed three more times, and then coverslipped. Immunostained sections were observed with a confocal laser-scanning microscope LSM510 META (Zeiss, Jena, Germany). dVenus fluorescence was readily detectable in fixed sections. However, when the counterstaining antibody required some pretreatment of the sections, dVenus was immunostained with a rabbit anti-GFP antibody. Sorted cells were spun down immediately onto poly-L-ornithine (15 μg/ml) and fibronectin (1 μg/ml) coated coverslips and immunostained by standard procedures. Post-stained cells were observed under a fluorescence microscope (Axiophoto; Zeiss). Primary antibodies against nestin (Rat401; Developmental Studies Hybridoma Bank of Iowa University), β-tubulin III, GFAP (Sigma), O4 (Chemicon, Temecula, CA), GFP (MBL, Woburn,

MA), Brn2 (Santa Cruz Biotechnology, Santa Cruz, CA), phospho-histone H3 (Cell Signaling Technology, Danvers, MA) and Group B1 SOX [SOX1-3; a kind gift from H. Kondoh, Ohsaka University (Tanaka et al., 2004)] were used according to the manufacturers' protocols.

### Flow cytometry

The cerebral wall of E14.5 transgenic or wild-type mouse embryos was dissected out into a chilled Hank's buffered saline solution, and suspended by brief mechanical treatment. One μg/ml of propidium iodide (PI) was added and the cells were filtered through a nylon mesh. Cell sorting and analysis were performed using MoFlo (Cytomation, Fort Collins, CO) with Summit software. Cells were analyzed for forward scatter, side scatter, PI fluorescence and dVenus or EGFP fluorescence with an argon laser (488 nm, 100 mW). Dead cells were excluded by gating on forward and side scatter, and by eliminating PI-positive events. Viable cells from the transgenic mice were sorted into ice-cold culture medium. Cells harvested from wild-type mice were used to set the background fluorescence.

### Determination of cell-cycle kinetics

Timed-pregnant female mice bearing transgenic embryos expressing dVenus were given thymidine analogues (50 μg/g body weight of the pregnant mouse) by intraperitoneal injection. The thymidine analogues, 5-bromo-2′-deoxyuridine (BrdU) and 5-iodo-2′-deoxyuridine (IdU) (Sigma-Aldrich), are incorporated into cells during the S phase of the cell cycle. The length of each cell-cycle stage in the dorsomedial region of the E14.5 mouse embryo was reported previously (Takahashi et al., 1995). On the basis of this report, we identified the cells that were labeled with IdU injected 3 hours before sacrifice as being in the G2-M phase. To overcome potential confusion from the long half-life of IdU, and to eliminate the labeling of cells remaining in G2-M phase, cells in the G1 phase were labeled with IdU 14.5 hours before sacrifice, when all the labeled cells had left the ventricular surface. Cells in the S phase were labeled by injecting BrdU 30 minutes before sacrifice in each trial. To detect BrdU and IdU, sections were pretreated with 2 M HCl for 5 minutes at room temperature, neutralized with 0.1 M Tris-HCl (pH 8.8) for 10 minutes, washed three times with PBS, and treated as described above for immunological staining from the blockage step. To detect IdU, an antibody that crossreacts with BrdU (Invitrogen) was used. The BrdU signal was distinguished from the IdU signal with an anti-BrdU-specific antibody (Abcam, Cambridge, MA).

### Reporter assays

An octamerized Nes30 sequence was fused to rabbit β-globin minimal promoter and inserted into the pGL3-Basic (Promega, Madison, WI) reporter vector. For reporter assays, NIH3T3 cells were cotransfected with 0.6 μg reporter, 10 ng effecter and reference pEF-LacZ (0.6 μg) using Lipofectamine Plus (Invitrogen). The amount of transfected DNA was equalized with empty vectors.

### Electrophoretic mobility shift assay

Flag-tagged Brn2 and Brn2 S362D were overexpressed in 293T cells. After 2 days, whole-cell lysates were prepared in a lysis buffer containing 10 mM Tris-HCl (pH 7.6), 50 mM NaCl, 30 mM sodium phosphate, 50 mM sodium fluoride, 20 mM β-glycerophosphate, 1% Triton X-100 and protease inhibitor mixture (Complete; Roche Applied Science, Basel, Switzerland). The sense and antisense Nes30 sequences were annealed and labeled with [$\gamma$-$^{32}$P]ATP (GE Healthcare, Piscataway, NJ) as a probe. The binding reaction was performed in a total volume of 25 μl binding buffer (50 mM HEPES-KOH pH 7.8, 250 mM KCl, 5 mM EDTA pH 8.0, 25 mM $MgCl_2$, 50% glycerol, and 25 mM DTT). Cell lysates were incubated for 30 minutes at room temperature with the labeled oligonucleotides. For the supershift assay, the binding product was incubated with an antibody against Flag (Sigma) for another 30 minutes. The samples were separated on native 8% polyacrylamide gels at 20 mA in Tris-borate EDTA buffer.

### Slice culture and DiI labeling

Slice culture and DiI labeling were performed as reported previously (Miyata et al., 2004). The cerebral cortex of E14.5 E/nestin:dVenus transgenic mouse embryos was labeled with DiI from the pial surface and sliced into coronal sections. Sections were embedded in collagen gel for time-lapse recording. The cultured slices were fixed in 4% paraformaldehyde for 15 minutes, vibratome sectioned and subjected to confocal microscopy to observe the dVenus expression in DiI-labeled cells.

We thank Hisato Kondoh for providing the rabbit anti-SOX1-3 antibody, Masaharu Ogawa for the Brn2 expression vector, and Miho Ohsugi for technical advice. This work was supported by a grant-in-aid from the Japanese Ministry of Education, Science, Sports and Culture of Japan (MEXT) and a grant from SORST, Japan Society for the Promotion of Science to H.O., the 21st Century COE program of MEXT to Keio University, and a grant from Bridgestone Corporation to K.S.

## References

**Bylund, M., Andersson, E., Novitch, B. G. and Muhr, J.** (2003). Vertebrate neurogenesis is counteracted by Sox1-3 activity. *Nat. Neurosci.* **6**, 1162-1168.

**Caelles, C., Hennemann, H. and Karin, M.** (1995). M-phase-specific phosphorylation of the POU transcription factor GHF-1 by a cell cycle-regulated protein kinase inhibits DNA binding. *Mol. Cell. Biol.* **15**, 6694-6701.

**Chou, Y. H., Khuon, S., Herrmann, H. and Goldman, R. D.** (2003). Nestin promotes the phosphorylation-dependent disassembly of vimentin intermediate filaments during mitosis. *Mol. Biol. Cell* **14**, 1468-1478.

**Cicero, S. and Herrup, K.** (2005). Cyclin-dependent kinase 5 is essential for neuronal cell cycle arrest and differentiation. *J. Neurosci.* **25**, 9658-9668.

**Corish, P. and Tyler-Smith, C.** (1999). Attenuation of green fluorescent protein half-life in mammalian cells. *Protein Eng.* **12**, 1035-1040.

**Fujita, S.** (1962). Kinetics of cellular proliferation. *Exp. Cell Res.* **28**, 52-60.

**Gaiano, N. and Fishell, G.** (2002). The role of notch in promoting glial and neural stem cell fates. *Annu. Rev. Neurosci.* **25**, 471-490.

**Hayes, N. L. and Nowakowski, R. S.** (2000). Exploiting the dynamics of S-phase tracers in developing brain: interkinetic nuclear migration for cells entering versus leaving the S-phase. *Dev. Neurosci.* **22**, 44-55.

**Herrmann, H. and Aebi, U.** (2004). Intermediate filaments: molecular structure, assembly mechanism, and integration into functionally distinct intracellular Scaffolds. *Annu. Rev. Biochem.* **73**, 749-789.

**Hinds, J. W. and Ruffett, T. L.** (1971). Cell proliferation in the neural tube: an electron microscopic and golgi analysis in the mouse cerebral vesicle. *Z. Zellforsch. Mikrosk. Anat.* **115**, 226-264.

**Hockfield, S. and McKay, R. D.** (1985). Identification of major cell classes in the developing mammalian nervous system. *J. Neurosci.* **5**, 3310-3328.

**Josephson, R., Muller, T., Pickel, J., Okabe, S., Reynolds, K., Turner, P. A., Zimmer, A. and McKay, R. D.** (1998). POU transcription factors control expression of CNS stem cell-specific genes. *Development* **125**, 3087-3100.

**Kamachi, Y., Uchikawa, M. and Kondoh, H.** (2000). Pairing SOX off: with partners in the regulation of embryonic development. *Trends Genet.* **16**, 182-187.

**Kapiloff, M. S., Farkash, Y., Wegner, M. and Rosenfeld, M. G.** (1991). Variable effects of phosphorylation of Pit-1 dictated by the DNA response elements. *Science* **253**, 786-789.

**Kawaguchi, A., Miyata, T., Sawamoto, K., Takashita, N., Murayama, A., Akamatsu, W., Ogawa, M., Okabe, M., Tano, Y., Goldman, S. A. et al.** (2001). Nestin-EGFP transgenic mice: visualization of the self-renewal and multipotency of CNS stem cells. *Mol. Cell. Neurosci.* **17**, 259-273.

**Kohyama, J., Tokunaga, A., Fujita, Y., Miyoshi, H., Nagai, T., Miyawaki, A., Nakao, K., Matsuzaki, Y. and Okano, H.** (2005). Visualization of spatiotemporal activation of Notch signaling: live monitoring and significance in neural development. *Dev. Biol.* **286**, 311-325.

**Lariviere, R. C. and Julien, J. P.** (2003). Functions of intermediate filaments in neuronal development and disease. *J. Neurobiol.* **58**, 131-148.

**Lendahl, U., Zimmerman, L. B. and McKay, R. D.** (1990). CNS stem cells express a new class of intermediate filament protein. *Cell* **60**, 585-595.

**Li, X., Zhao, X., Fang, Y., Jiang, X., Duong, T., Fan, C., Huang, C. C. and Kain, S. R.** (1998). Generation of destabilized green fluorescent protein as a transcription reporter. *J. Biol. Chem.* **273**, 34970-34975.

**Lothian, C. and Lendahl, U.** (1997). An evolutionarily conserved region in the second intron of the human nestin gene directs gene expression to CNS progenitor cells and to early neural crest cells. *Eur. J. Neurosci.* **9**, 452-462.

**Marvin, M. J., Dahlstrand, J., Lendahl, U. and McKay, R. D.** (1998). A rod end deletion in the intermediate filament protein nestin alters its subcellular localization in neuroepithelial cells of transgenic mice. *J. Cell Sci.* **111**, 1951-1961.

**Miyata, T. and Ogawa, M.** (2007). Twisting of neocortical progenitor cells underlies a spring-like mechanism for daughter-cell migration. *Curr. Biol.* **17**, 146-151.

**Miyata, T., Kawaguchi, A., Okano, H. and Ogawa, M.** (2001). Asymmetric inheritance of radial glial fibers by cortical neurons. *Neuron* **31**, 727-741.

**Miyata, T., Kawaguchi, A., Saito, K., Kawano, M., Muto, T. and Ogawa, M.** (2004). Asymmetric production of surface-dividing and non-surface-dividing cortical progenitor cells. *Development* **131**, 3133-3145.

**Nagai, T., Ibata, K., Park, E. S., Kubota, M., Mikoshiba, K. and Miyawaki, A.** (2002). A variant of yellow fluorescent protein with fast and efficient maturation for cell-biological applications. *Nat. Biotechnol.* **20**, 87-90.

**Noctor, S. C., Flint, A. C., Weissman, T. A., Dammerman, R. S. and Kriegstein, A. R.** (2001). Neurons derived from radial glial cells establish radial units in neocortex. *Nature* **409**, 714-720.

**Noctor, S. C., Flint, A. C., Weissman, T. A., Wong, W. S., Clinton, B. K. and Kriegstein, A. R.** (2002). Dividing precursor cells of the embryonic cortical ventricular zone have morphological and molecular characteristics of radial glia. *J. Neurosci.* **22**, 3161-3173.

**Okano, H.** (2002). Stem cell biology of the central nervous system. *J. Neurosci. Res.* **69**, 698-707.

**Pekny, M., Johansson, C. B., Eliasson, C., Stakeberg, J., Wallen, A., Perlmann, T., Lendahl, U., Betsholtz, C., Berthold, C. H. and Frisen, J.** (1999). Abnormal reaction to central nervous system injury in mice lacking glial fibrillary acidic protein and vimentin. *J. Cell Biol.* **145**, 503-514.

**Rakic, P.** (1972). Mode of cell migration to the superficial layers of fetal monkey neocortex. *J. Comp. Neurol.* **145**, 61-83.

**Rakic, P.** (2003). Elusive radial glial cells: historical and evolutionary perspective. *Glia* **43**, 19-32.

**Reynolds, B. A. and Weiss, S.** (1996). Clonal and population analyses demonstrate that an EGF-responsive mammalian embryonic CNS precursor is a stem cell. *Dev. Biol.* **175**, 1-13.

**Sahlgren, C. M., Mikhailov, A., Hellman, J., Chou, Y. H., Lendahl, U., Goldman, R. D. and Eriksson, J. E.** (2001). Mitotic reorganization of the intermediate filament protein nestin involves phosphorylation by cdc2 kinase. *J. Biol. Chem.* **276**, 16456-16463.

**Sahlgren, C. M., Mikhailov, A., Vaittinen, S., Pallari, H. M., Kalimo, H., Pant, H. C. and Eriksson, J. E.** (2003). Cdk5 regulates the organization of Nestin and its association with p35. *Mol. Cell. Biol.* **23**, 5090-5106.

**Sauer, M. E. and Walker, B. E.** (1959). Radiographic study of interkinetic nuclear migration in the neural tube. *Proc. Soc. Exp. Biol. Med.* **101**, 557-600.

**Segil, N., Roberts, S. B. and Heintz, N.** (1991). Mitotic phosphorylation of the Oct-1 homeodomain and regulation of Oct-1 DNA binding activity. *Science* **254**, 1814-1816.

**Steinert, P. M., Chou, Y. H., Prahlad, V., Parry, D. A., Marekov, L. N., Wu, K. C., Jang, S. I. and Goldman, R. D.** (1999). A high molecular weight intermediate filament-associated protein in BHK-21 cells is nestin, a type VI intermediate filament protein. Limited co-assembly in vitro to form heteropolymers with type III vimentin and type IV alpha-internexin. *J. Biol. Chem.* **274**, 9881-9890.

**Takahashi, T., Nowakowski, R. S. and Caviness, V. S., Jr** (1993). Cell cycle parameters and patterns of nuclear movement in the neocortical proliferative zone of the fetal mouse. *J. Neurosci.* **13**, 820-833.

**Takahashi, T., Nowakowski, R. S. and Caviness, V. S., Jr** (1995). The cell cycle of the pseudostratified ventricular epithelium of the embryonic murine cerebral wall. *J. Neurosci.* **15**, 6046-6057.

**Tanaka, S., Kamachi, Y., Tanouchi, A., Hamada, H., Jing, N. and Kondoh, H.** (2004). Interplay of SOX and POU factors in regulation of the Nestin gene in neural primordial cells. *Mol. Cell. Biol.* **24**, 8834-8846.

**Tokunaga, A., Kohyama, J., Yoshida, T., Nakao, K., Sawamoto, K. and Okano, H.** (2004). Mapping spatio-temporal activation of Notch signaling during neurogenesis and gliogenesis in the developing mouse brain. *J. Neurochem.* **90**, 142-154.

**Tsai, J. W., Chen, T., Kriegstein, A. and Valle, R. B.** (2005). LIS1 RNA interference blocks neural stem cell division, morphogenesis, and motility at multiple stages. *J. Cell Biol.* **170**, 935-945.

**Tsai, J. W., Bremner, K. H. and Valle, R. B.** (2007). Dual subcellular roles for LIS1 and dynein in radial neuronal migration in live brain tissue. *Nat. Neurosci.* **10**, 970-979.

**Xie, Z., Moy, L., Sanada, K., Zhou, Y., Buchman, J. and Tsai, L.** (2007). Cep120 and TACCs control interkinetic nuclear migration and the neural progenitor pool. *Neuron* **56**, 79-93.

**Yasui, Y., Goto, H., Matsui, S., Manser, E., Lim, L., Nagata, K.-i. and Inagaki, M.** (2001). Protein kinases required for segregation of vimentin filaments in mitotic process. *Oncogene* **20**, 2868-2876.

**Zimmerman, L., Parr, B., Lendahl, U., Cunningham, M., McKay, R., Gavin, B., Mann, J., Vassileva, G. and McMahon, A.** (1994). Independent regulatory elements in the nestin gene direct transgene expression to neural stem cells or muscle precursors. *Neuron* **12**, 11-24.

# 電子線〈フリーズレプリカ〉トモグラフィー法による細胞膜骨格の3次元イメージング

諸根　信弘[a]，臼倉　治郎[b]，楠見　明弘[c]

[a]国立精神・神経センター神経研究所，[b]名古屋大学エコトピア研究所，[c]京都大学再生医科学研究所

キーワード：細胞膜，膜骨格，フリーズレプリカ，電子線トモグラフィー

## 1. はじめに：細胞膜の構造

細胞膜の厚さは，わずか約5 nm．このため，多くの場合，細胞膜は2次元的構造と考えられている．さらに，この構造は液体の性質を持ち，細胞膜の構成分子は，細胞膜の中でブラウン運動している．このような運動ができるからこそ，例えば，シグナル分子はお互いに衝突し，シグナルを伝えることができると考えられている．このような細胞膜の動的構造は，シンガー・ニコルソンの流動モザイクモデル（1972）として教科書に掲載され，細胞膜の基本概念となっている[1]．その後，膜分子の運動解析・シミュレーションにより，細胞膜には，仕切りが入っていて[2〜6]，細胞膜における分子運動は流動モザイクモデルだけでは説明できないことが明らかになってきた．細胞膜の仕切りは，細胞膜の細胞質側表面を覆っているアクチン線維のネットワーク，「膜骨格（membrane skeleton）」でできていることが提案されている[7,8]．

赤血球の膜骨格については，古くから構造解析が進められてきた．これは細胞質を除いたゴースト膜が簡単に単離できるため，膜骨格の生化学的・構造的な研究が簡単だったためである．この赤血球の膜骨格は，他の細胞のそれとは大きく異なっている．アクチンは，トロポミオシンに結合して，12〜18個のGアクチンからなる40 nm程度の長さの短い線維を作り，これが細胞膜上に杭のように結合している．結合先は，膜貫通型タンパク質のグリコフォリンCとバンド4.1複合体である．この短いアクチン線維の杭の間をスペクトリンという鎖状分子の四量体が繋いでいる．すなわち，短いアクチン線維の杭が，スペクトリン四量体をメッシュワーク状に組み立てて膜骨格を構築し[9〜14]，それが赤血球に柔軟性と剛性を与えている．

リンパ球では，細胞膜の直下から厚さ2〜3 μmにわたってアクチン線維のネットワークがびっしりと存在している．これは「皮質アクチン（cortical actin）」と呼ばれている[15]．これらのアクチンフィラメントは赤血球の40 nm程度の短い線維ではなく，マイクロメートルの桁の長さになっている．非常に多くのアクチン結合タンパク質が，これらのアクチンの側面どうしをつないで，アクチンフィラメントを束化したり，70°の角度で分岐させたり，直角に結合させたりしている．このようなアクチンフィラメントのネットワークが赤血球と異なって細胞膜の細胞質側表面から細胞質へと3次元的に広がっている．この皮質アクチンが，リンパ球に，変形能や血管での耐力性を与えていると考えられる．血小板の膜骨格は，細胞膜上の糖タンパク質複合体やゲルゾリンの皮質アクチンへの結合を媒介していると考えられ，主成分はスペクトリンだと考えられているが，スペクトリンの分布はまだ観察されていない[16,17]．

非血球系では，小腸上皮組織の細胞膜直下に形成された膜骨格が，広川—Heuserグループによって，急速凍結・ディープエッチング・白金レプリカ法を用いて，膜骨格研究の非常に初期に明らかにされ，有名である[18,19]．細胞膜表面の微繊毛の内部には，アクチンフィラメントの束が構築されていて，その先端部が，微繊毛の先に結合し，根元では「terminal web」と呼ばれる構造に結合して，そこから，アクチン，ミオシン，中間径フィラメントからなる細胞骨格に繋がっている．これは，違う種類のフィラメントの微細構造の特徴や特異的ラベリング法により同定されて明らかになった．

哺乳動物の通常の培養細胞では，1980年代から膜直下の細胞質側表面に線維が存在することが分かっていており，アクチン線維が含まれることがわかっていた．しかし，線維の細胞膜上での分布，その主成分，線維の作る構造の特徴などはほとんど分かっていなかった．これを明らかにするためには，細胞膜を広く剥離して，その細胞質側表面を露出させる

Nobuhiro Morone, Jiro Usukura and Akihiro Kusumi: Three dimensional imaging of the plasma membrane skeleton as revealed by freeze-replica and electron tomography

[a]〒187-8502　東京都小平市小川東町4-1-1
E-mail: morone@ncnp.go.jp
[b]〒464-8603　名古屋市千種区不老町1-1
E-mail: usukuraj@esi.nagoya-u.ac.jp
[c]〒606-8507　京都市左京区聖護院川原町
E-mail: akusumi@frontier.kyoto-u.ac.jp

2007年10月4日受付

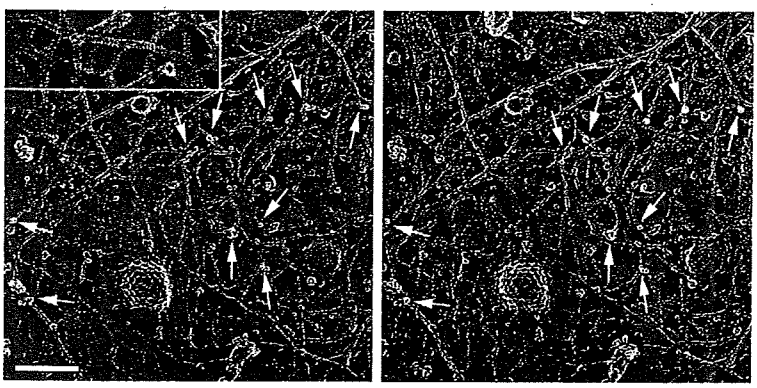

図1　膜骨格のディープエッチング像．ラット由来の線維芽細胞のアピカル細胞膜の細胞質側表面を観察した．無数のフィラメント構造が重なってメッシュワークを形成している．クラスリン被覆ピット（多格子模様）やカベオラ（渦巻き模様）の膜陥入構造が観察されることから，膜直下であることがわかる．1本1本の線維は約5 nmごとのストライプ模様を表す（拡大図）ことから，膜骨格はおもにアクチンフィラメントからなることがわかる．細胞質側表面に広がって形成される膜骨格から細胞質側への繋がり（矢印）も観察されることから，膜骨格が細胞質内部の細胞骨格とも繋がって，3次元的なネットワークを構築していることが分かる．スケールバーは，100 nm.

方法，観察された線維を同定する方法などの開発が必要であった．最近になって，筆者らは，急速凍結ディープエッチ免疫レプリカ電顕法と電子線トモグラフィー法の併用により，アクチンフィラメントを主成分とする分子ネットワークが細胞膜全体にわたって，細胞質側表面から数十ナノメートルの領域を覆っていることを，高分解能の電子顕微鏡観察により見出した（図1）[20]．フリーズレプリカ試料を電子線トモグラフィーに適用する，電子線〈フリーズレプリカ〉トモグラフィー法は，世界に先駆けた可視化技術であり，世界的にも非常に大きな注目を集めている．さらに，この新しい可視化法による膜骨格の3次元再構築構造により，最初に述べた細胞膜の仕切り[20～22]は，アクチン膜骨格によるものであることが強く示唆された．この研究について，概説する．

## 2. 膜骨格の3次元可視化法

### 2.1 細胞膜全体を剥離する方法

まず，培養皿に培養した細胞の上側（培養液側）の細胞膜の細胞質側を観察する方法を開発した（図2）．このためには，細胞の上から，低分子量のカチオン化試薬であるアルシアンブルーでコートした小さいカバーグラスを置き，細胞膜を結合させた後に，カバーグラスを剥がす，という操作をおこなう．試料調製法を細かく工夫することによって，ディープエッチング法で，アピカル側の細胞膜の約1/4程度の大きさの膜断片が，ほとんどいつも観察できるようになった．免疫金コロイド標識（免疫レプリカ）によって膜骨格がどのようなタンパク質で形成されているのかも調べることができた（図3）．

培養ディッシュへの接着面（ベーサル側）の細胞膜の観察には，プローブ型の低出力超音波発生装置を利用する[23]．これによって，上側の細胞膜と細胞質の大部分を吹き飛ばす．最初，この方法では観察できる領域が狭く，部分的に膜骨格のメッシュワーク構造が壊れて，定量的評価が難しかった．カベオラのような小さな膜陥入構造の観察にも，注意深い試料調製が必要とされた．しかし，最近になって筆者らは直径1ミリ程度のプローブを数ミリワット以下の出力で使用することで，細胞の底面側の細胞質側表面全面で膜骨格やカベオラ・ピットを可視化できるようになった．

従来，細胞膜直下の皮質フィラメントを可視化するためには，界面活性剤（Triton-X100やPolyethylene glycol）による細胞膜の可溶化がおこなわれてきた．しかし，この方法ではカベオラやピットなどの膜裏打ち構造は観察されない．これまでに，血小板や魚のケラトサイト（ケラチン生成細胞，鱗の根元にある細胞）などで，皮質アクチンの形成が明瞭に観察されている[16,17,24,25]．

### 2.2 急速凍結法

細胞質側表面が露出した細胞膜を，次に細胞質側から急速凍結させる．細胞の上側の細胞膜を剥がして観察するにしても，下側に残った細胞膜を観察するにしても，細胞膜の外側表面は，ガラスに結合している．このガラスを上にし，細胞膜の細胞質側表面を下にして，液体ヘリウムで冷却した純銅ブロックの鏡面に圧着させる（メタルコンタクト法）ことにより，細胞膜を急速凍結させる．純銅ブロックの鏡面は，ダイヤモンドペーストで研磨して準備する．この凍結方法では，純銅の高い熱伝導率が液化ヘリウム温度付近で最大となる性質も利用している．極めて急速（$10^5$°C/秒）に温度降下がおきるため，圧着面から20ミクロン程度の領域では氷晶形成が生じることなく，良好な凍結が得られる（図2）．

### 2.3 ディープエッチング法とフリーズレプリカ法

凍結試料は，凍ったまま超高真空（$10^{-6}$ Pa程度）の装置に入れて，ダイアモンドナイフなどで，試料表面の氷などを削る．一番具合の良いところでは，細胞膜から0.2-1ミクロン程度の厚さの領域が，ガラス上に残るようにする．さらにこの試料の温度をやや上昇させて，−100～−70°Cくらいにし，表面から，氷を昇華させ，細胞膜上の構造が深いところまで氷の上に露出するようにする（1 μm程度）．これをディープエッチング（deep etching）と呼んでいる．凍結割断法では細胞膜脂質二分子層の真中で細胞膜が割れた所（細胞膜中央の疎水面）を観察するのに対して，ディープエッチング法では，もっと表面の構造を，水を昇華させることによって露出させて観察する．

ディープエッチング後に，白金・炭素を1～2 nmの厚さで低角度（20度程度）回転蒸着する．細胞膜上の構造があると，そこには白金粒子が降り積もり，それによってコントラストを付けることができる．チャンバー内の真空度を上

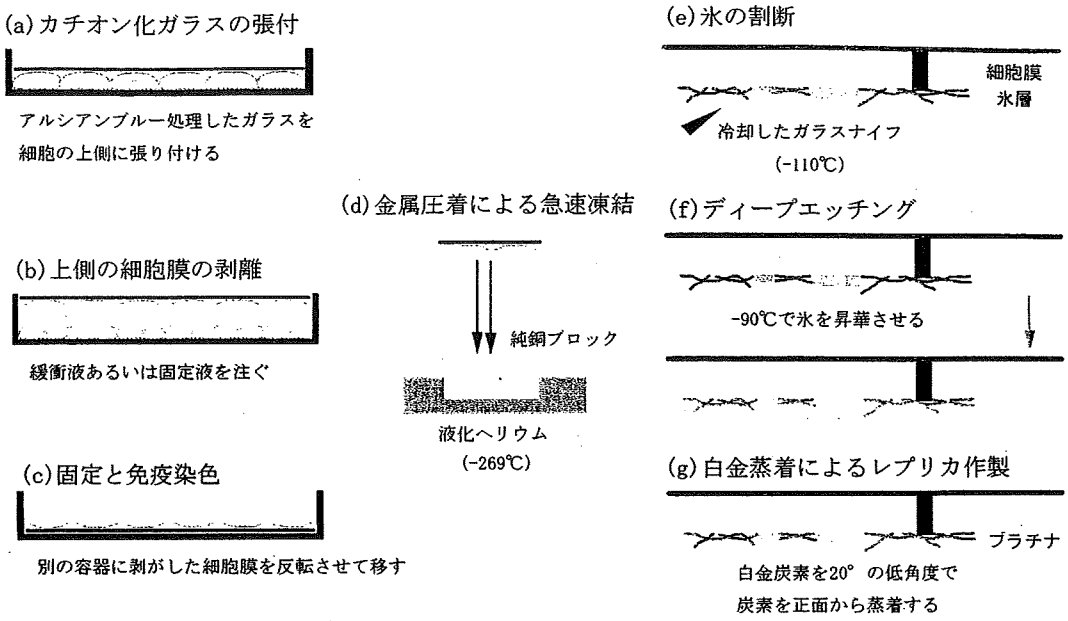


図2　細胞質側表面にある膜骨格の可視化法．(a) プラスチックシャーレに培養された細胞を緩衝液で2回洗浄する．自然乾燥しない程度まで水分を取り除いた後，アルシアンブルーでカチオン化処理したカバーガラスをアピカル側の細胞膜表面に乗せる．(b) 固定液（あるいは緩衝液だけ）をゆっくりシャーレの縁から注ぎ，ガラスが浮く力によって細胞膜を剥離させ，細胞質側表面を裸出させる．(c) さらに固定した後，緩衝液で洗浄する．この段階では，裸出した細胞質側表面に対して，免疫金コロイド染色によって分子標識することも可能である．さらに蒸留水で洗浄後，(d) 細胞質側表面の水分を，自然乾燥が生じない程度まで濾紙で吸収し，液化ヘリウムで浸した純銅ブロックの鏡面に圧着させ，急速凍結する．次に，(e) -110度まで冷却したガラスナイフで凍結面を割断する．(f) チャンバー温度を-90度まで上昇させて，割断面から1 μm以上の部分をディープエッチングさせる．(g) 白金・炭素は低角度（20度程度）で，次の補強用の炭素は正面（90度）から回転蒸着を行い，「細胞膜の裏打ち構造」のレプリカ膜を調製する．(d) ～ (g) は本文も参照．

げ，試料ステージの温度を下げることにより，プラチナ粒子が細かくなり，より微細な構造を反映したレプリカが調製できる（図2）．

### 2.4 電子線トモグラフィー

基盤とする電子線コンピュータトモグラフィーは90年代に自動化され，現在，研究室で実施されている．

透過型電子顕微鏡を用いた電子線トモグラフィーの原理は，病気の診断で使われるエックス線断層撮影と基本的に同じで，エックス線源を電子線に換えて，微細な構造が見えるようにしたものと考えて良い．すなわち，試料を電子線に対して傾け，一つの視野に対して傾きが異なった画像を多数撮影し，これから，計算によって試料のスライス像を計算によって求める（図4a）．この方法は90年代から自動化され，細胞内部の微細構造を定量的に観察する方法として発展してきた[26～30]．この過程で，以下の3つの主要な要素技術の開発がおこなわれ，現在のように普及し始めるに至った．①サイドエントリー型試料傾斜ホルダーとZ軸補正が可能なトモグラフィー電子顕微鏡の開発，②高感度・高精度CCDカメラの開発，③これらを連動させて，自動的に連続傾斜像を撮影するソフトウェアの開発である．

我々は，細胞膜直下を電子線トモグラフィーにより定量的に可視化し，膜骨格が細胞膜と接している部分の構造を解明しようとした．実際の手順としては，まず，細胞質側を裸出させた膜試料の同一視野について，±70°範囲で，1°毎に，傾斜像をCCDカメラで位置補正しながら，合計141枚撮影する（図4a）．次に，これをもとに，計算によって，0.85 nmのスライス厚で120枚程度の連続スライス像を求め，3次元再構築をおこなう．連続傾斜像から連続スライス像への変換計算は，コロラド大学ボールダー校のMcIntosh博士らが開発した演算プログラム「IMOD」[31]で，連続スライス像から3次元構造の再構築はTemplate Graphics社製の「AMIRA」を，我々は用いている．

## 3. 細胞膜の細胞質側表面は，全面にわたってアクチン膜骨格で覆われている

上記のように，細胞膜の非常に広い範囲にわたって，ディープエッチング電子顕微鏡観察を一気におこなうことができるようになった．それらの結果をまとめて述べる．まず，クラスリン被覆ピット（直径が約200 nmの多角格子模様[32]）やカベオラ（直径が約50～80 nmのストライプ模様[33]）がきわめて明瞭に観察され（図1），細胞膜の細胞質側表面が同定できた．また，その表面に，フィラメントのネットワークが観察できた．アクチン線維は，モノマーであるGアクチンの配列により，約5.5 nmピッチのストライプ模様[28]が理想的な場合には観察されることが分かっていた[20]．しかし，これが見えるのは，以前は，ほとんどin

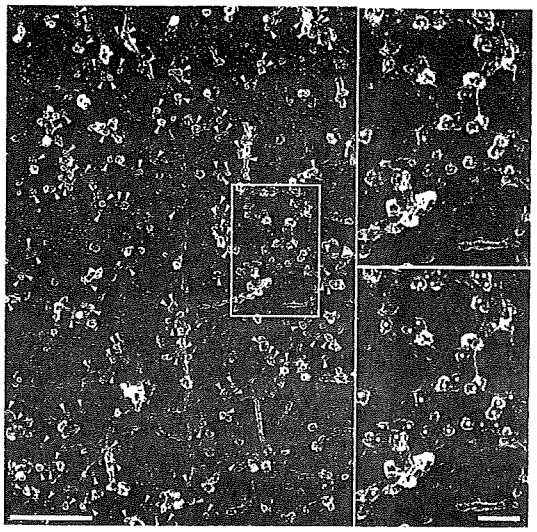

図3　膜骨格はアクチンフィラメントからなる．アクチンプローブの免疫金コロイド（5 nmϕ）で標識した細胞膜のレプリカ像．膜骨格フィラメント上に並んでいる白い小さな点がプローブである（矢印）．白くはっきりした点の周囲にハロが見えるのが金コロイドプローブの特徴である（上拡大図）．金コロイドが黄色で強調されている（下拡大図）．スケールバーは100 nm である．

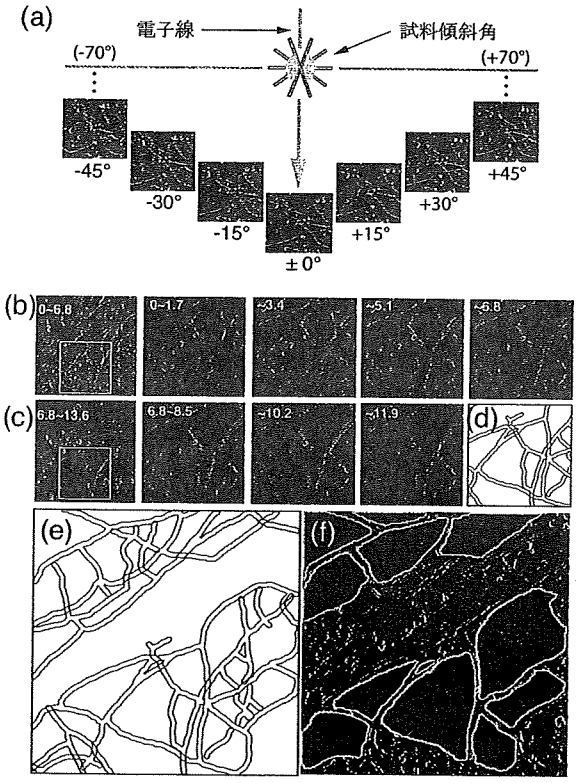


図4　電子線トモグラフィーにより細胞膜骨格を3次元的に選択した．(a) 筆者らは同一視野に対して±70度の試料傾斜角度範囲を1度ステップで連続撮影した合計141枚のCCD画像をインテグレートしている．これらの連続傾斜像からzスライス像を計算により求める．最終的には，それらの連続スライス像と細胞質側表面からの部分的立体再構築像［(b) 0～6.8 nmや (c) 6.8～13.6 nmの範囲を1.7 nmごとに計算した像群］を相互に比較することで，細胞質側表面に再近接したフィラメント群を選択して，これらを「細胞膜直下の膜骨格」と決定した．(d, e) の緑色で縁取りされたフィラメントが細胞質側表面に，また赤色が細胞質に接近して局在していることが分かった．そのため，この緑色の成分が「細胞膜骨格」であり，この膜骨格で囲まれた領域［(f) 黄色で縁取りされ，緑色で塗られたところ］が，細胞膜のコンパートメントである．

vitroで調製されたアクチン線維であり，細胞中では，まれに，少数の線維が，5.5 nmピッチのストライプを示す程度であった．我々は，試料調製条件を細かく調整し，細胞膜上のほとんど全ての線維は，5.5 nmピッチのストライプを示すことを証明した．これによって，膜骨格のほとんどは，アクチン線維から構成されていることが明らかになった．

試料を急速凍結する前に，免疫金コロイドで標識すると，ディープエッチング像で金コロイド粒子を観察することにより，見えている構造の構成分子が同定できる．本研究では，アクチンに結合する免疫金コロイド標識（直径5 nm）をおこなった．膜骨格を形成するフィラメント上に，金コロイド標識が並んで観察され，上記の5.5 nm毎のストライプパターンに加えて，膜骨格がアクチンでできていることが再確認された（図3）．併せて，これまでにスペクトリン，アンキリン，フィラミン，テーリン，アデューシン，Arp2/3なども，線維上に同定されている．すなわち，膜骨格はアクチン線維を主成分とし，それに多数のアクチン結合タンパク質が結合してできていることがわかった[20]．細胞質側表面に並行に広がる膜骨格から細胞質側への繋がりも観察され（図1矢印），膜骨格のネットワークが細胞質内部の細胞骨格とも繋がって，3次元的な広がりがあることが分かってきた．

## 4. 膜骨格により細胞膜はコンパートメント化されている

最近，「細胞膜が膜骨格とそこに結合した膜貫通型タンパク質で仕切られている」という，細胞膜の流動モザイクモデルをさらに深化させた「新しい細胞膜構造モデル」[6]が提唱されている．このモデルを検証するため，細胞膜直下の膜骨格のメッシュサイズの分布と，リン脂質の拡散から推定されるコンパートメントの大きさの分布を比較した．アクチン線維は，白金蒸着試料では，太さ（厚さ）が約10 nm程度になる．そこで，細胞膜の細胞質側表面から10 nm程度の厚さに局在するアクチンフィラメントを3次元再構築像において同定した（図4，5）．これらが，細胞膜分子の側方拡散運動に影響を与える膜骨格構造と考えられるからである．細胞質側表面から1.7 nmごとの部分的な3次元構築像（図4b, c）や0.85 nm毎の連続スライス像のムービーにより，フィラメントの3次元的な位置を識別した．図4d, eで，緑の線維は細胞膜から10 nm以内に局在する線維であり，赤の線維は，その上に載っている線維である．緑の線維で囲まれた領域が，細胞膜上での膜骨格で囲まれたメッシュであると考えられるので（図4f），その領域の面積を多数測定しヒストグラムにした（図5）．このヒストグラムを，脂質の高速

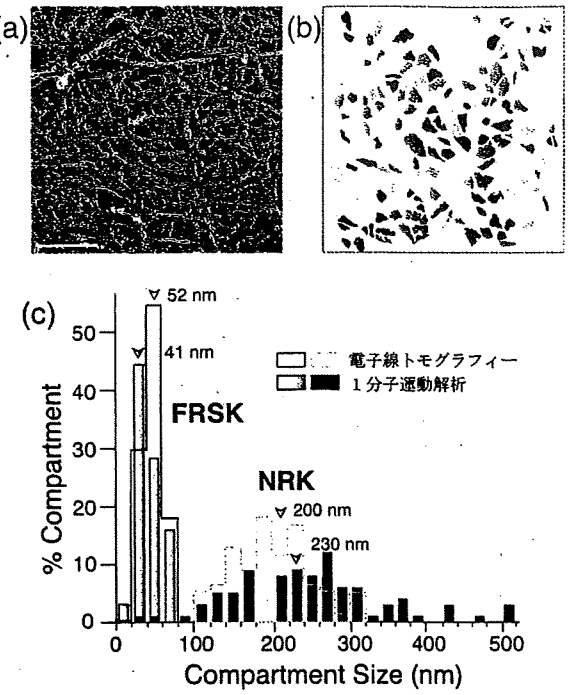


図5　電子線トモグラフィーと1分子運動解析で細胞膜のコンパートメントサイズが一致した．急速凍結・ディープエッチング法で観察した細胞質側表面（a）には，膜骨格のメッシュワークで囲まれた膜コンパートメント（b）が存在することがわかった．色分けされた領域が1つ1つの膜コンパートメントを表している．（c）2種類の細胞（FRSKとNRK細胞）で電子線トモグラフィーと超高速カメラによる1分子運動解析で決定したコンパートメントサイズを比較してみると，平均値と中央値を含めてヒストグラム表示全体でほぼ一致した．スケールバー：100 nm.

1分子追跡によって求めた，膜分子に対する拡散障壁によるコンパートメントサイズ[20~22]と比較した．そうすると，これらは，2種類の全くコンパートメントの大きさが異なる細胞（NRKとFRSK細胞）でほぼ一致した．これは，「膜骨格フェンスモデルおよび膜骨格にアンカーされた膜貫通型タンパク質のピケットモデル」を強く支持するものである．

## おわりに

急速凍結・ディープエッチ・白金蒸着によるレプリカ法と，電子線トモグラフィー法との組み合わせにより，細胞膜の構造の定量的研究は，大きく進んだ．この方法を様々な細胞に，また，刺激前後での変化の検討に応用することにより，膜骨格の機能解析がさらに大きく進むことが期待される．

謝　辞：本研究の遂行にあたり，（株）三菱化学生命科学研究所の瀬藤光利先生，国立精神・神経センター神経研究所の湯浅茂樹先生，米国ワシントン大学医学部のジョン・ホイザー先生にお世話になりました．謹んでお礼を申し上げます．

## 文　献

1) Singer, S.J. and Nicolson, G.L.: *Science*, 175, 720-731 (1972)
2) Sheetz, M.P.: *Semin. Hematol.*, 20, 175-188 (1983)
3) Saxton, M.J.: *Biophys. J.*, 55, 21-28 (1989)
4) Edidin, M., Kuo, S.C. and Sheetz, M.P.: *Science*, 254, 1379-1382 (1991)
5) Kusumi, A. and Sako, Y.: *Curr. Opin. Cell Biol.*, 8, 566-574 (1996)
6) Kusumi, A., Nakada, C., Ritchie, K., Murase, K., Suzuki, K., Murakoshi, H., Kasai, R.S., Kondo, J. and Fujiwara, T.: *Annu. Rev. Biophys. Biomol. Struct.*, 34, 351-378 (2005)
7) Luna, E.J. and Hitt, A.L.: *Science*, 258, 955-964 (1992)
8) Jacobson, K., Sheets, E.D. and Simson, R.: *Science*, 268, 1441-1442 (1995)
9) Tsukita, S., Tsukita, S. and Ishikawa, H.: *J. Cell Biol.*, 85, 567-576 (1980)
10) Branton, D., Cohen, C.M. and Tyler, J.: *Cell*, 24, 24-32 (1981)
11) Mohandas, N. and Evans, E.: *Annu. Rev. Biophys. Biomol. Struct.*, 23, 787-818 (1994)
12) Byers, T.J. and Branton, D.: *Proc. Natl. Acad. Sci. USA*, 82, 6153-6157 (1985)
13) Bennett, V.: *Physiol. Rev.*, 70, 1029-1065 (1990)
14) Takeuchi, M., Miyamoto, H., Sako, Y., Komizu, H. and Kusumi, A.: *Biophys. J.*, 74, 2171-2183 (1998)
15) Bornens, M., Paintrand, M. and Celati, C.: *J. Cell Biol.*, 109, 1071-1083 (1989)
16) Hartwig, J.H., Chambers, K.A. and Stossel, T.P.: *J. Cell Biol.*, 108, 467-479 (1989)
17) Hartwig, J.H. and DeSisto, M.: *J. Cell Biol.*, 112, 407-425 (1991)
18) Hirokawa, N. and Heuser, J.E.: *J. Cell Biol.*, 91, 399-409 (1981)
19) Hirokawa, N., Tilney, L.G., Fujiwara, K. and Heuser, J.E.: *J. Cell Biol.*, 94, 425-443 (1982)
20) Morone, N., Fujiwara, T., Murase, K., Kasai, R.S., Ike, H., Yuasa, S., Usukura, J. and Kusumi, A.: *J. Cell Biol.*, 174, 851-862 (2006)
21) Fujiwara, T., Ritchie, K., Murakoshi, H., Jacobson, K. and Kusumi, A.: *J. Cell Biol.*, 157, 1071-1081 (2002)
22) Murase, K., Fujiwara, T., Umemura, Y., Suzuki, K., Iino, R., Yamashita, H., Saito, M., Murakoshi, H., Ritchie, K. and Kusumi, A.: *Biophys. J.*, 86, 4075-4093 (2004)
23) Heuser, J.: *Traffic*, 1, 545-552 (2000)
24) Svitkina, T.M., Verkhovsky, A.B., McQuade, K.M. and Borisy, G.G.: *J. Cell Biol.*, 139, 397-415 (1997)
25) Stossel, T.P., Condeelis, J., Cooley, L., Hartwig, J.H., Noegel, A., Schleicher, M. and Shapiro, S.S.: *Nat. Rev. Mol. Cell Biol.*, 2, 138-145 (2001)
26) Fung, J.C., Liu, W., de Ruijter, W.J., Chen, H., Abbey, C.K., Sedat, J.W. and Agard, D.A.: *J. Struct. Biol.*, 116, 181-189 (1996)
27) Perkins, G.A., Renken, C.W., Song, J.Y., Frey, T.G., Young, S.J., Lamont, S., Martone, M.E., Lindsey, S. and Ellisman, M.H.: *J. Struct. Biol.*, 120, 219-227 (1997)
28) Medalia, O., Weber, I., Frangakis, A.S., Nicastro, D., Gerisch, G. and Baumeister, W.: *Science*, 298, 1209-1213 (2002)
29) McIntosh, R., Nicastro, D. and Mastronarde, D.: *Trends Cell Biol.*, 15, 43-51 (2005)
30) Lucic, V., Forster, F. and Baumeister, W.: *Annu. Rev. Biochem.*, 74, 833-865 (2005)
31) Kremer, J.R., Mastronarde, D.N. and McIntosh, J.R.: *J. Struct. Biol.*, 116, 71-76 (1996)
32) Heuser, J.E. and Anderson, R.G.: *J. Cell Biol.*, 108, 389-400 (1989)
33) Rothberg, K.G., Heuser, J.E., Donzell, W.C., Ying, Y.S., Glenney, J.R. and Anderson, R.G.: *Cell*, 68, 673-682 (1992)
34) Heuser, J.E. and Kirschner, M.W.: *J. Cell Biol.*, 86, 212-234 (1980)